Liftoff and Transition Database Generation for Launch Vehicles Using Data-Fusion-Based Modeling

T.J. Wignall*
NASA Langley Research Center, Hampton, VA 23681, USA

A data fusion technique for merging multiple data sources with differing fidelity and resolution was developed to support the production of aerodynamic lineload databases for the Liftoff and Transition (LOT) flight phase of the Space Launch System (SLS). The technique uses a reduced order model based on a high-fidelity lineload dataset from Computational Fluid Dynamics (CFD) to predict solutions for a much larger solution space. Even higher-fidelity force and moment information (from wind-tunnel tests) is then used to adjust the model. The adjustment uses constrained optimization through the method of Lagrange multipliers in order to minimize the deviation of the lineload distribution from the spatially-dense CFD solution, while ensuring that the integrated force and moment values match those observed in physical wind tunnel measurements. Though the wind-tunnel data are operationally-dense (available at many flow conditions), they are spatially coarse (as only the overall forces and moments are available). Conversely, CFD for such complex configurations is expensive, and thus operationally sparse. Data fusion techniques are necessary to make the most efficient use of available information, delivering accurate results within time and resource constraints.

I. Nomenclature

a	=	ROM Coefficient
$\hat{a}$	=	DFROM Coefficient
λ	=	Legrange Multiplier
C_p	=	Pressure coefficient
C_f	=	Friction coefficient
C_{f_x}	=	Friction coefficient in x direction
C_{f_y}	=	Friction coefficient in y direction
C_{f_z}	=	Friction coefficient in z direction
C_X	=	Force coefficient in x direction
C_Y	=	Force coefficient in y direction
C_Z	=	Force coefficient in z direction
C_{A_P}	=	Axial component of the resultant force acting on the vehicle
C_{N_P}	=	Normal component of the resultant force acting on the vehicle
C_{Y_P}	=	Side force component of the resultant force acting on the vehicle
S	=	Solution across the surface of a vehicle component
Ψ	=	Principal Component across the entire surface of the vehicle
Δc	=	Contribution of a principal component to a force or moment
R	=	Covariance matrix
V	=	Matrix composed of columns of eigenvectors
$\hat{V}$	=	Inverse of the matrix composed of columns of eigenvectors

Acronyms

DFROM	=	Data Fused Reduced Order Model
LOT	=	Liftoff and Transition
LOO	=	Leave One Out

*Aerospace Engineer, Configuration Aerodynamics Branch, Mail Stop 499.

PCA = Principal Component Analysis
PC = Principal Component
ROM = Reduced Order Model
SLS = Space Launch System
SRB = Solid Rocket Booster

II. Introduction

The NASA Space Launch System (SLS) is a new series of launch vehicles being designed for deep space exploration. For an in-depth introduction and update on SLS analysis see the work by Pinier, Herron, and Gomez [1]; however, a brief overview is presented here to provide context for this work. The SLS has several different configurations, which allow it the flexibility to accomplish a variety of missions, but all of them are made up of a central core and two solid rocket boosters (SRBs), a port and starboard. The differences between the configurations are the choice in upper stages along with whether it is configured to carry the Orion spacecraft or cargo in a fairing. The variety in the SLS configurations can be seen in Fig. 1.

The present work focuses on the development of lineload databases for the liftoff and transition (LOT) portion of the Block 1B configurations, both crew and cargo. For reference, the transition domain covers all total angle of attack, α_P, and roll, ϕ_P, combinations in flow below Mach 0.3, a large domain that is mostly incompressible. The liftoff portion of the database includes the launch tower and is neglected here. Lineloads are the spatially distributed forces across the axial direction of the vehicle that are primarily used in structural analysis and have secondary uses for guidance, navigation, and control [2].

Lineloads databases are different from conventional force and moment aerodynamic databases because of their spatial distribution across the vehicle. This need for spatial distribution means that CFD is the best tool available. As outlined in more depth in the work by Ratnayake, Krist, and Ghaffari [3], the LOT domain is a difficult flow condition to model using common finite volume flow solvers. Because of the size of the SLS vehicles, high angle of attack with large

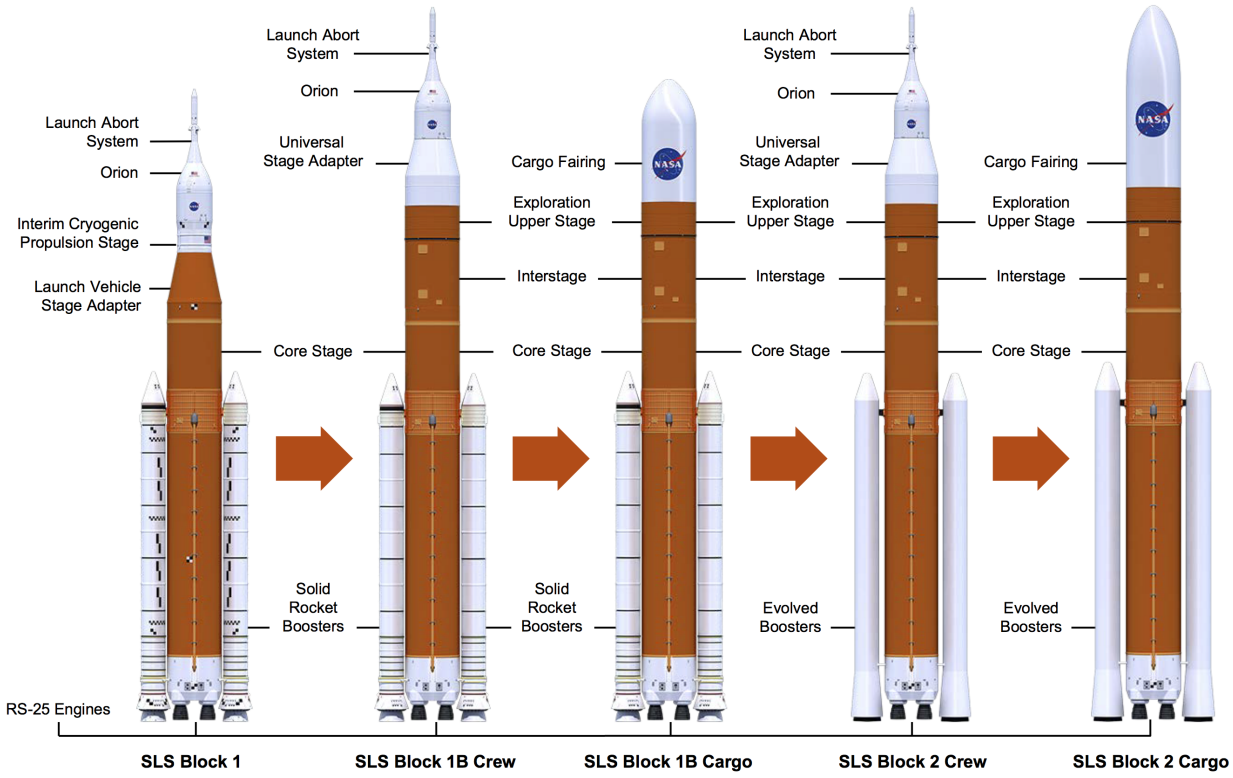

Fig. 1 The Various configurations of the Space Launch System.

regions of separated flows, and each point being a major commitment of computational resources, significant effort was put into getting the most out of each CFD run. Based on the results and work of Carlson et al. [4], the decision to once again augment the CFD with a reduced order model (ROM) was made with the eventual goal of incorporating data assimilation to improve the final database. The focus of the paper is on methods of ROM generation and the techniques developed to create a data-fused reduced order model (DFROM).

To help guide the CFD and check its quality, wind tunnel data from tests in the NASA Langley 14- by 22-Foot Subsonic Tunnel are examined and used [5]. These data are broken up into two parts. The first part, which is used more extensively, is the data that gets processed into the force and moment database. Due to the addition of load cells in the SRBs, force and moment data now exist for all three components of the vehicle and not just the total vehicle unlike previous testing, which only provided total vehicle forces and moments. The primary use of these data is data assimilation; however, it was also used in CFD point selection, as well as a quality check on the CFD and ROM outputs. The secondary part of the wind tunnel data is pressure port reading. This was used as a secondary check on the CFD and ROM data; however, because of the addition of the load cells, there are only pressure port data for the core on the configurations of interest. The force and moment database generated from the wind tunnel testing is considered of higher fidelity than CFD because of CFD's historical shortfalls when trying to capture flows with large wake regions. Because of the availabilty of higher fidelity data, techniques to augment the CFD derived lineloads by the force and moment database is highly valuable.

Adjustment of integrated lineload values is also of interest because current database generation methods create a disconnect between force and moment databases and the forces that the lineloads represent. By fusing the lineload data with the force and moment database, it is possible to remove this disconnect. Another method to adjust lineloads is being developed using similar techniques by Dalle [6], which differs from the current work primarily by starting from the lineloads instead of the surface pressures. This method makes some things simpler but loses some information on how the forces and moments are coupled when applying the adjustments.

This paper is split into two major sections. The first explores the creation of the ROM and the lineloads it generates. The second part explores the adjustment of the ROM to a DFROM and the new lineloads based on that adjustment. The standard SLS axis system is presented in Fig. 2 for reference. Since the roll varies across all 360° and the total angle of attack goes from 0° to 90°, the aerodynamic analysis for the LOT domain is done in missile axis to smooth out trends across the large changes in flow direction. The asymmetric vortices that appear at higher angles of attack are another reason the analysis stays in the missile axis system. These vorticies are common to all slender bodies in medium to high angle-of-attack flows and many resources have been devoted to characterizing and modeling them over the years [7, 8]. These vorticies make drawing trends and predictions for side force and yawing moment difficult because under slightly different conditions both CFD modeling, and to a lesser extent wind tunnel testing, can see evidence of the asymmetric vortices moving from one side of the vehicle to the other. By analyzing the data in the missile axis, the primary effect is seen in the side force and yawing moment, which makes analysis of trends in the other forces and moments more reliable.

III. Reduced Order Model

A ROM is a mathematical model derived from a sequence of high fidelity observations or simulations, that preserves the essential physics and predictive capability of the original data set but can be interrogated at a much lower computational cost. In this work, the high fidelity observations from which the ROM is built are time-averaged CFD results generated in Kestrel [9] with details explained in [3]. These are then used to produce a ROM that can approximate the surface grid solution at any angle of attack and roll combination. This method is solver independent and in theory could be implemented using solutions from multiple solvers. The major requirement is that all the solutions are on a common grid, which can be accomplished through interpolation.

The model generation is split into two parts, basis extraction and recombination. Principal component analysis (PCA) (aka proper orthogonal decomposition) [10] is used as a means to extract the basis of the desired solution space. The extracted basis, the principal components (PCs), are then linearly recombined to provide an approximation of the CFD solution at new conditions. The results for the ROM are then compared to wind tunnel data and CFD check points to prove its predictive capability.

A. Model Development

Since the force and moment database is split by component (core and the two SRBs), the ROM is split into the three vehicle components. These components do not interact with each other once split, so the first step is splitting the CFD results into these components. For reference, a typical pressure distribution from CFD is presented in Fig. 3. As can

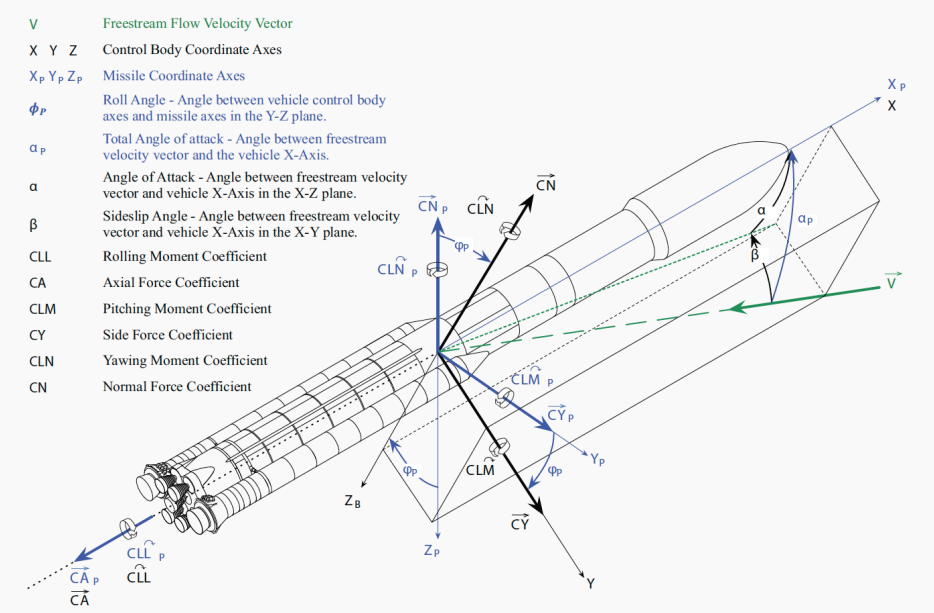

Fig. 2 The standard reference frames used for the SLS program.

be seen on the upper surface, there are large regions of separation, as previously mentioned, that make this problem difficult to solve numerically.

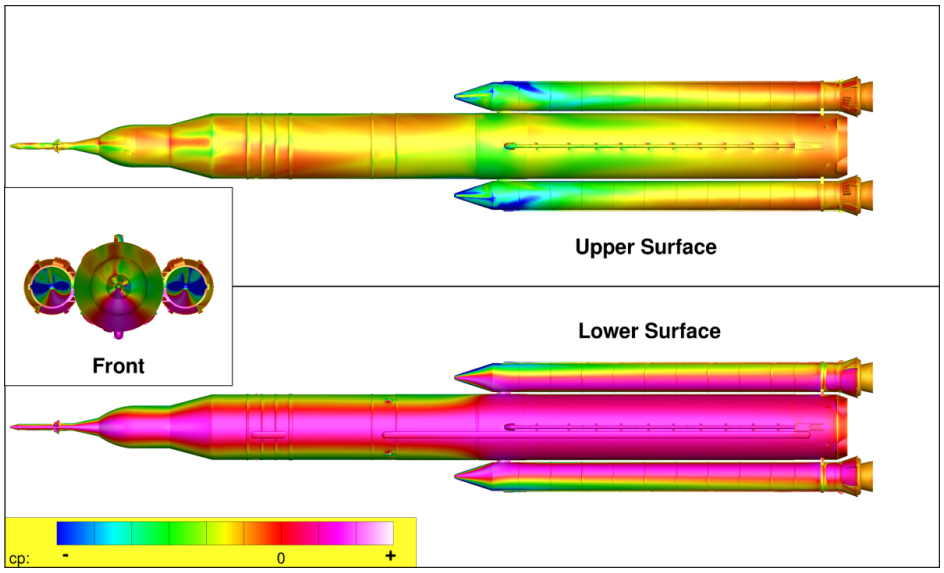

Fig. 3 Time-averaged surface coefficient of pressure distribution of Block 1B crew vehicle at $\alpha_P = 50°$, $\phi_P = 0°$.

This solution is then split into the three vehicle components: core, port SRB and starboard SRB, and then integrated to get the sectional loads as seen in Fig. 4. The top graph contains the sectional forces acting in the axial direction, the middle graph contains the sectional forces acting in the side direction, and the bottom contains sectional forces in the normal direction. Below is the outline of the launch vehicle for reference. The thin grey dashed line represents zero to help give reference. The x-axis in the figure coincides with the x-axis of the SLS system. For comparison purposes, the normal force and the side force lineloads have the same scale. This will be consistent of all future normal and side force related plots. As mentioned in the introduction, the aerodynamic analysis for the LOT domain is in the missile axis system, which becomes more important at other roll angles.

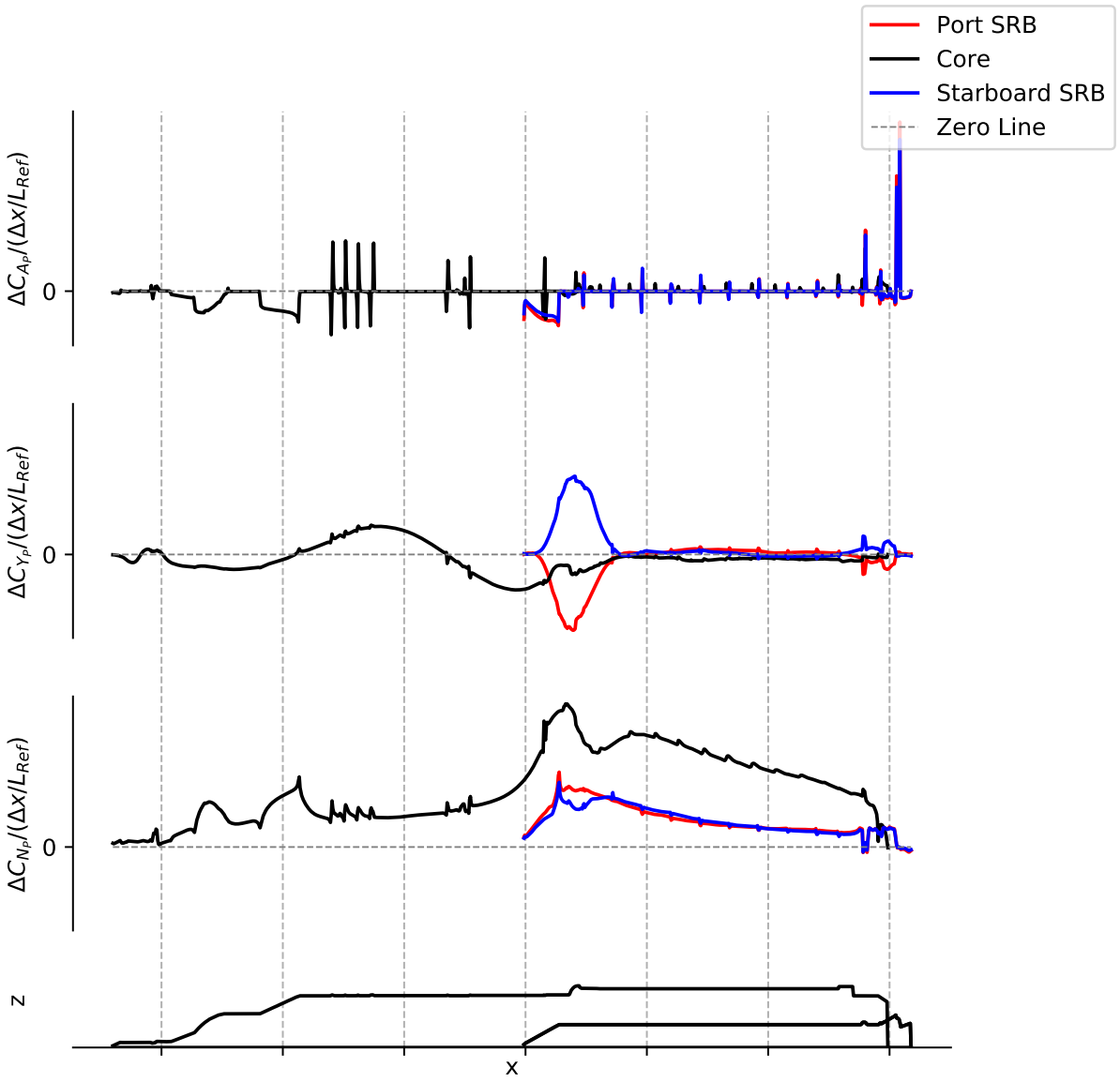

Fig. 4 CFD Lineloads for Block 1B crew vehicle at α_P = 50°, ϕ_P = 0°.

These two figures (Fig. 3 and 4) represent the desired output of the ROM. The surface allows for further analysis of the flow physics in the LOT domain which would not be possible due to resource constraints if only CFD was available, and the lineloads are the data being delivered in the databases.

Once the CFD data are gathered and split up, PCA is used for feature extraction. There are many techniques available that can be used to extract features, but PCA was selected due to its simplicity and its use in previous work. The friction and pressure are kept separate during the PCA portion of the ROM creation to allow for the ability to analyze how the ROM predicts viscous contributions separate from the pressure components. This also allows for the ability to adjust them independently as seen later. For a given component, such as the core, the CFD solutions are split into 4 matrices, S, (one for each variable) with rows of cells and columns of solutions similar to the example presented in Fig. 5.

These matrices are then used to find the covariance matrix of the solutions, which is computed as follows:

$$R_{i,j}^{l,k} = cov(S_i^{l,k}, S_j^{l,k}) \tag{1}$$

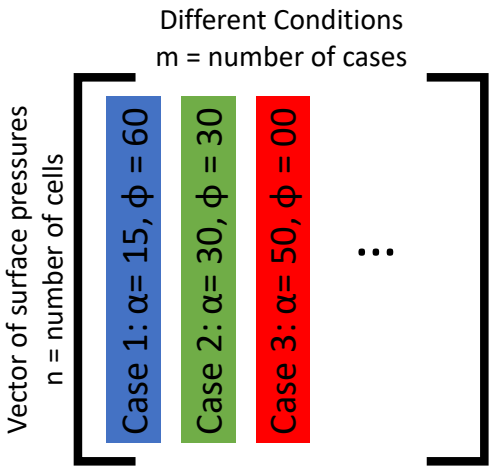

Fig. 5 Setup of matrix used in PCA.

where S_i and S_j represent the surfaces from distinct CFD solutions, k represents the component under consideration (core, port SRB, or starboard SRB), and l represents the variable under consideration (C_P, C_{F_x}, C_{F_y}, or C_{F_z}). The resulting covariance matrices, $R^{l,k}$, are square matrices that are sized based on the number of input CFD solutions. That is, if 21 CFD cases are used, $R^{l,k}$ would be a 21×21 matrix. For reference, 21 CFD cases were used in the development of the Block 1B crew vehicle and 60 for the Block 1B cargo configuration. This difference in number of points used was primarily due to the available computational resources and the increased complexity of flow around the Block 1B cargo vehicle. The database generated for the Block 1B crew vehicle was generated from data generated for one quadrant and reflected to the other quadrants while the database for the cargo vehicle relied on data from all 4 quadrants.

Once the 12 covariance matrices (3 components with 4 variables each) are found, the next step is to calculate their eigenvalues and eigenvectors. The eigenvectors are needed to transform the matrix of CFD solutions into PC space while the eigenvalues are used later in the data fusion portion. The surface distribution Ψ of a given PC is defined by:

$$\Psi_j^{l,k} = \sum_{i=1}^{n} V_{i,j}^{l,k} S_i^{l,k} \tag{2}$$

where the sum is taken over the input CFD solutions and $V^{l,k}$ are the eigenvectors of the covariance matrix $R^{l,k}$. There is one set of PCs for each variable and component.

The nature of PCA orders the new PCs by the amount of variance they contribute to the system. This relative importance is reflected by the eigenvalues, which are plotted in Fig. 6. The eigenvalues are normalized by the sum of the eigenvalues within variables for the Block 1B crew vehicle and then plotted againt the PC number. The values on the x-axis correspond to the numbering of the PCs. This demonstrates how the first few PCs dominate the construction of the ROM surfaces. The first three PCs related to pressure contain almost 90% of the total pressure in the system. Since the normalizations are within variables, the difference between the eigenvalues of the different variables is lost. The smallest pressure eigenvalue is an order of magnitude greater than the largest eigenvalue that corresponds to friction.

After converting to PC space, PC surfaces can be plotted as presented in Fig. 7, which shows the first PC related to pressure on the core of the Block 1B crew configuration. Since PC space is outside of the LOT domain, there is no corresponding angle of attack or roll angle. This surface shows large features, and could easily be mistaken for the surface from a CFD solution. As the PC number goes up, the feature sizes decrease and the overall surface becomes less like a CFD surface solution due to the lack of coherent structures.

Lineloads allow for easier comparison between multiple surfaces and so integrating PC surfaces into lineloads gives an idea of the shapes that individual PCs will contribute to the lineloads. An example of these lineloads can be seen in Fig. 8. Figure 8 shows various PC lineloads corresponding to the integrated surface pressures for the Block 1B crew configuration including the PC shown in Fig. 7. PC lineloads are not in the missile axis system since they are outside of the LOT domain and as such the lineloads do not show axial, side and normal force but X, Y, and Z directional forces. In the SLS system, these are identical to the body axis forces; however, since the analysis and other results shown are in missile axis the distinction is made here to stress the difference. While integration into sectional forces hides some of

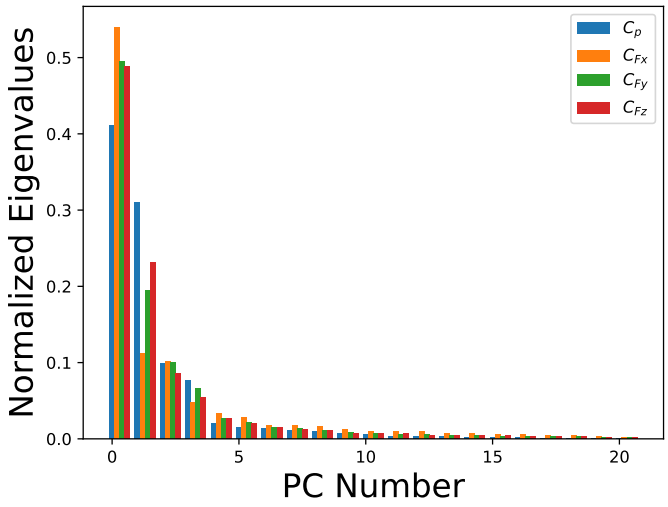

Fig. 6 Normalized eigenvalues of the four variables for the core of the Block 1B crew vehicle.

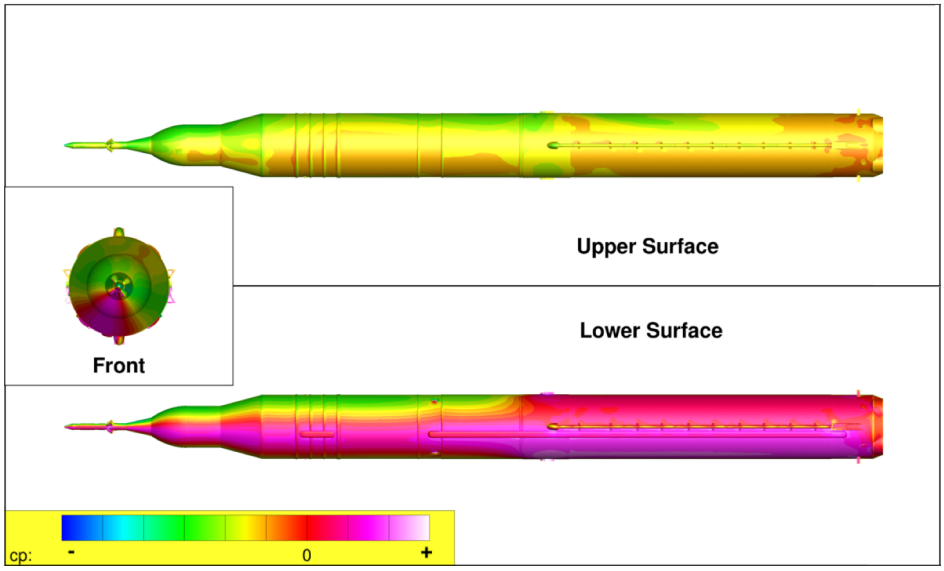

Fig. 7 Surface distribution of the first Principal Component related to pressure on the core of the Block 1B crew configuration.

the lack of coherence of the underlying surfaces, it is still clear that the higher numbered PCs tend to contribute much less to the output than the lower numbered ones. This further reinforces the results of the eigenvalue analysis above.

By taking the inverse of the definition of the PCs in Eq. 2, a linear combination of the PCs can be used to recover the original CFD solution surfaces,

$$S_j^{l,k} = \sum_{i=1}^{n} \hat{V}_{i,j}^{l,k} \Psi_i^{l,k} \tag{3}$$

where $\hat{V}$ is the inverse of the matrix of eigenvectors. The next step is to modify this equation to allow for calculating solution surfaces at conditions outside the CFD run matrix. This is done through replacing the inverse of the eigenvector

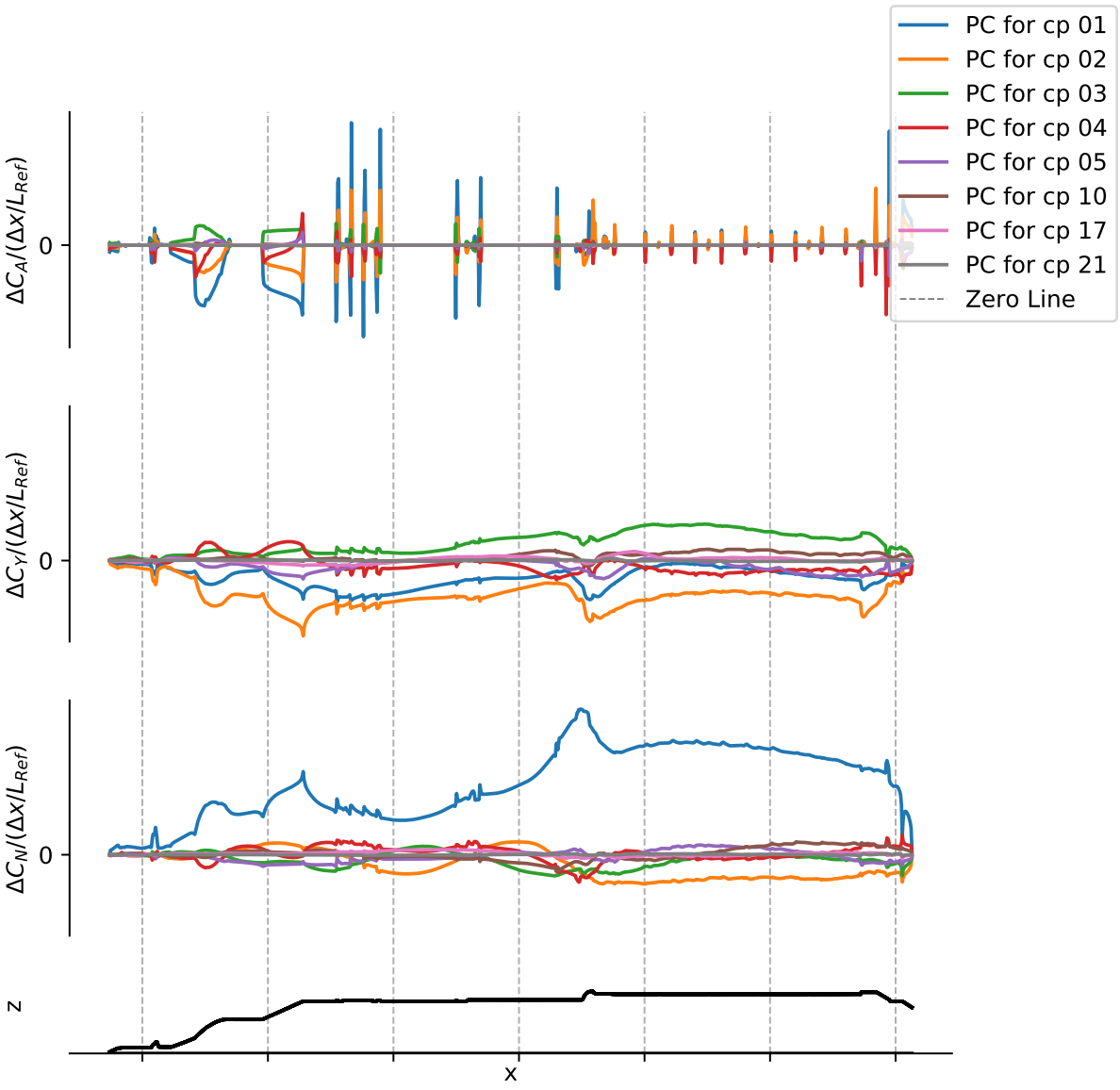

Fig. 8 PC distributions related to pressure integrated into lineloads on the core of the Block 1B crew configuration.

with a coefficient, a, which is a function of α_P and ϕ_P.

$$S^{l,k}(\alpha_P, \phi_P) = \sum_{i=1}^{n} a_i^{l,k}(\alpha_P, \phi_P) \cdot \Psi_i^{l,k} \tag{4}$$

The remaining piece of the puzzle is to determine the ROM coefficients a, which apply proper weighting to each PC in the sum in order to arrive at the surface for each condition. The most straight forward way to get the necessary values for a, is to take the inverted values from the matrix of eigenvectors and assign them to the corresponding conditions of the CFD solution. From those handful of scattered points, the rest of the domain is calculated through interpolation. An example distribution of the ROM coefficient can be seen in Fig. 9, which shows the first ROM coefficient associated with pressure on the core of the Block 1B crew vehicle as a function of angle of attack and roll. The circles show where

there were originating CFD data in the domain. As can be seen, the coefficient is generally smooth with a peak in one corner (top left). As the PC number increases, the coefficients tend to get more peaks and valleys and as a result are less smooth.

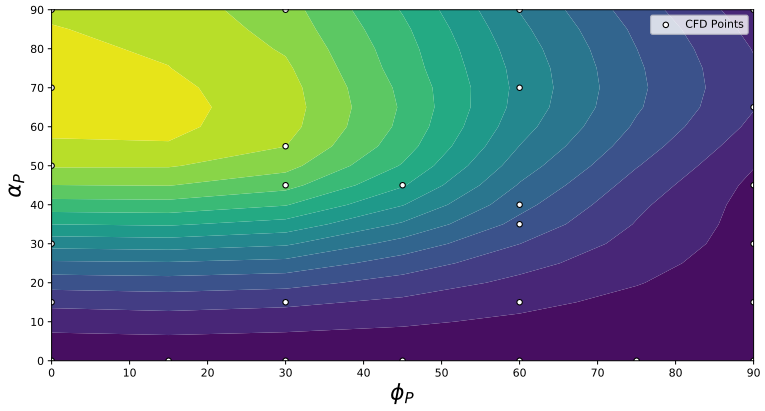

Fig. 9 The values for the first ROM coefficient for pressure across α_P and ϕ_P for the core of the Block 1B crew vehicle. The dots represent locations of CFD points.

At this point, the basic ROM is complete. The model can take in desired angle of attack and roll conditions and return an approximation of a CFD surface as desired. A benefit to this form of ROM is that since the ROM coefficients are a function of condition only (and not any spatial variable), they can be removed from spatial integration. While the entire surface can be used to check for quality, only the lineloads are needed for the final database. With the ability to integrate the PCs spatially, this allows for smaller datasets to be saved while keeping the ability to fully create the database.

B. Model Results

Once the ROM coefficients and PC surfaces are calculated, it is possible to start outputting surfaces. The pressure surface in Fig. 10 is the output of the ROM for the Block 1B crew configuration at $\alpha_P = 60°$ and $\phi_P = 0°$. This condition is relatively close to the condition shown in Fig. 3 and so similarities are expected and this holds true. The most noticeable and most important is the increased area of separation as the angle of attack increases. Additionally, on the upper surface, despite the core and SRBs being calculated separately, there are flow structures that emanate from the SRB noses and continue onto the core. This shows that the ROM maintains at least some of the physics of the original CFD. This level of analysis is possible since the ROM is built off and recreates entire surfaces and not just lineloads or forces and moments.

Since it is now possible to output surfaces at any condition desired, the ability to check each output quickly becomes overwhelming. As mentioned in the introduction, the availability of wind tunnel data allows for a check of quality. A typical force and moment comparison can be seen in Fig. 11 and Fig. 12. Force and moment data for the Block 1B crew configuration as a function of angle of attack at $\phi_P = 0°$ are seen in Fig. 11. Similar data at $\phi_P = 120°$ for the Block 1B cargo configuration are seen in Fig. 12. The black symbols represent data gathered from wind tunnel testing, the red circles are the data from CFD, while the line represents the output of the ROM. The top half of the figures are, from left to right, the axial, normal, and side force coefficients of the entire vehicle. The bottom half of the figures are, from left to right, the rolling, pitching, and yawing moment coefficients of the entire vehicle. The data shown are for the total vehicle, which means they compare the three component ROMs added together to data derived from the balance reading. As in previous plots, the normal force and side force coefficient plots have the same scale. The same holds true for the pitching and yawing moment coefficient plots. These figures show that the ROM exactly reconstructs the integrated force and moment coefficients generated from the CFD results. This is expected since the ROM coefficients are defined by the inverse of the eigenvector matrix. It also shows that the ROM is able to generate the same overall trends of the wind tunnel data. The locations that the ROM misses are also areas that the CFD misses, which are the mismatches that prompted the exploration of data fusion techniques. The biggest of these mismatches are the side force

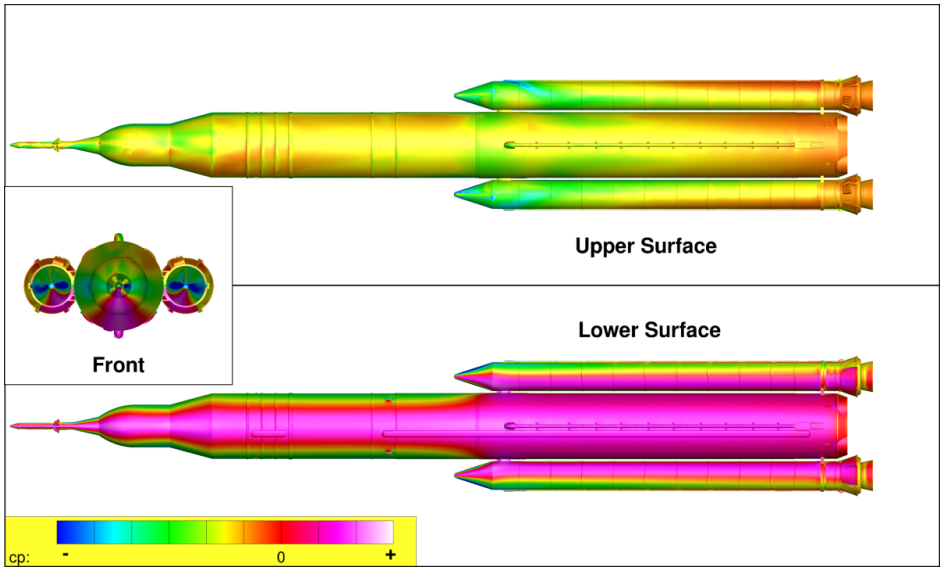

Fig. 10 ROM output of surface pressures for the Block 1B crew at α_P = 60° and ϕ_P = 0°.

and yawing moment coefficients, which are an effect of the asymmetric vortices as displayed for the Block 1B crew forces and moments. The other important trend is that the CFD tends to underpredict peak normal and pitching moment coefficient values as displayed by the Block 1B cargo data. While rolling moment coefficents look to be poorly matched for the Block 1B crew vehicle, those values are very small and the level of disagreement is on the same order as the rolling moment coefficients seen in the Block 1B cargo vehicle.

As another check on the ROM's ability to recreate CFD level quality, leave one out (LOO) analysis was done. To clarify, the ROM was recreated while leaving one of the contributing CFD cases out, which could then be used as a check. The new dropped point ROM was compared to the ROM at the CFD condition that was dropped to examine the ROM's sensitivity to missing information, as well as being able to compare it to CFD data. As a reminder, the ROM exactly recreates the CFD data when at a point with CFD. Two example cases are presented through lineload comparisons. The Block 1B crew vehicle shown in Fig. 13 shows a flip in the vortex prediction as seen in the side force sign change based on dropping the CFD point at α_P = 50°, ϕ_P = 0°. This sign flip does not move the dropped point ROM outside the realm of CFD-like data since CFD was able to recreate the vortex on either side by changing settings. The Dropped Point ROM prediction for the normal force accurately recreates the forebody portion of the full ROM almost exactly, with only slight differences near the aft end. The axial force lineload has relatively little change except a general decrease in axial force coefficient near the aft end, which mirrors the changes observed near the aft end in the other lineloads. Overall, the dropped point ROM for this case confirms the ROM's ability to approximate CFD solutions.

The Block 1B cargo vehicle result shown in Fig. 14 shows one of the worst cases that was encountered at α_P = 45°, ϕ_P = 270°. Here once again, there is a vortex prediction flip when dropping the CFD point, however, the effects are much greater in this case. Since the whole surface is effected by the vortex flip, the changes in the normal force can also be attributed to this especially since most of the changes are in the middle section of the vehicle forward of the SRBs, which is the section of the vehicle that is affected most by the forebody vortices. Despite being a considerably different form, the integrated values for the ROM and the dropped point ROM are fairly similar. This demonstrates that while the ROM may not always reproduce CFD data as accurately as desired, it can adequately give an approximation of what the CFD would produce.

A ROM was developed that is able to provide results at a variety of conditions that compare favorably to CFD results and database forces and moments. This was demonstrated through comparison to the wind tunnel force and moment database where it captures the trends seen while keeping some of the shortcomings in the base CFD. The robustness of the ROM is demonstrated through LOO analysis that shows that the ROM can adequately recreate CFD data.

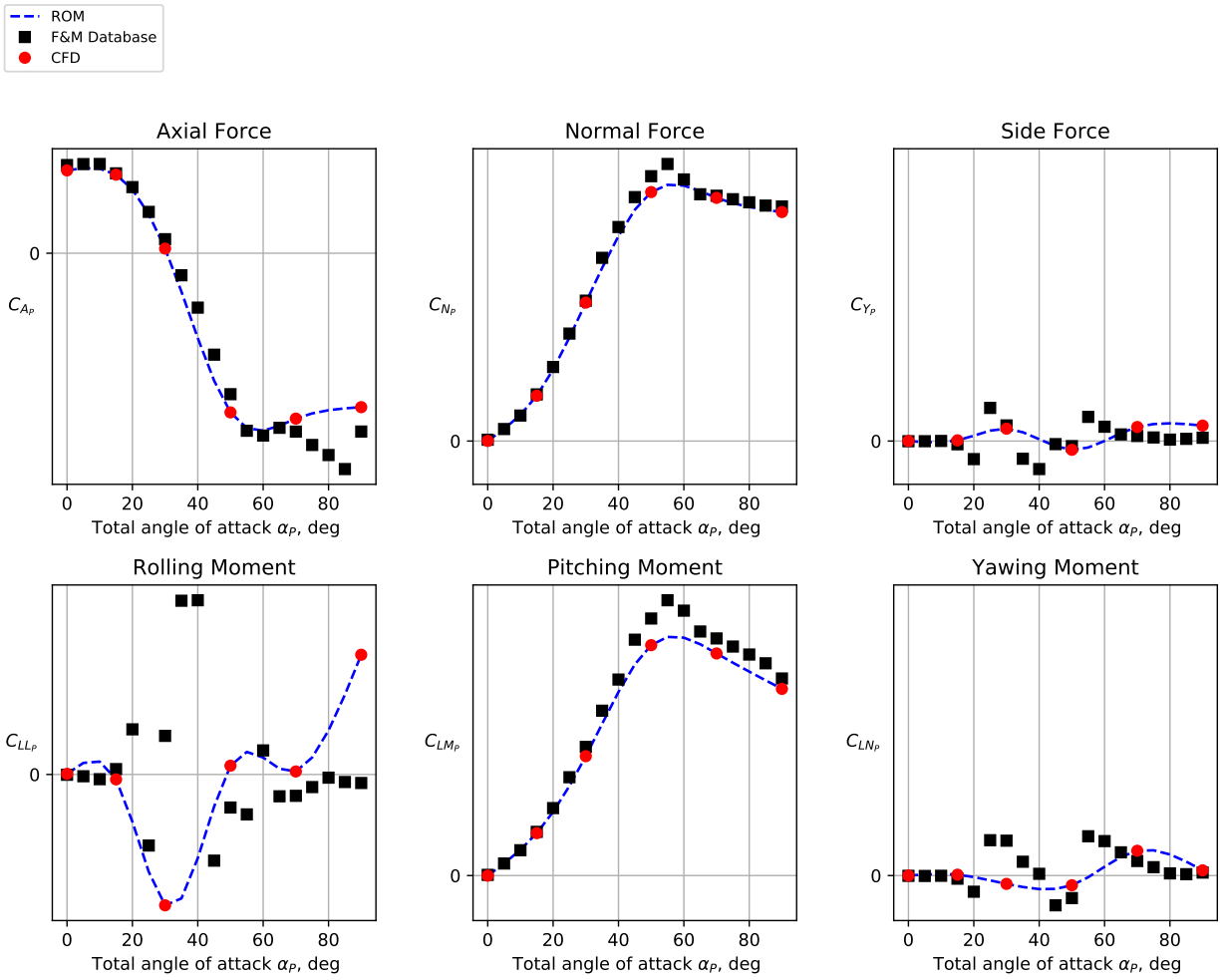

Fig. 11 Comparison of wind tunnel force and moment coefficients versus angle of attack at $\phi_P = 0^\circ$ for the Block 1B crew vehicle.

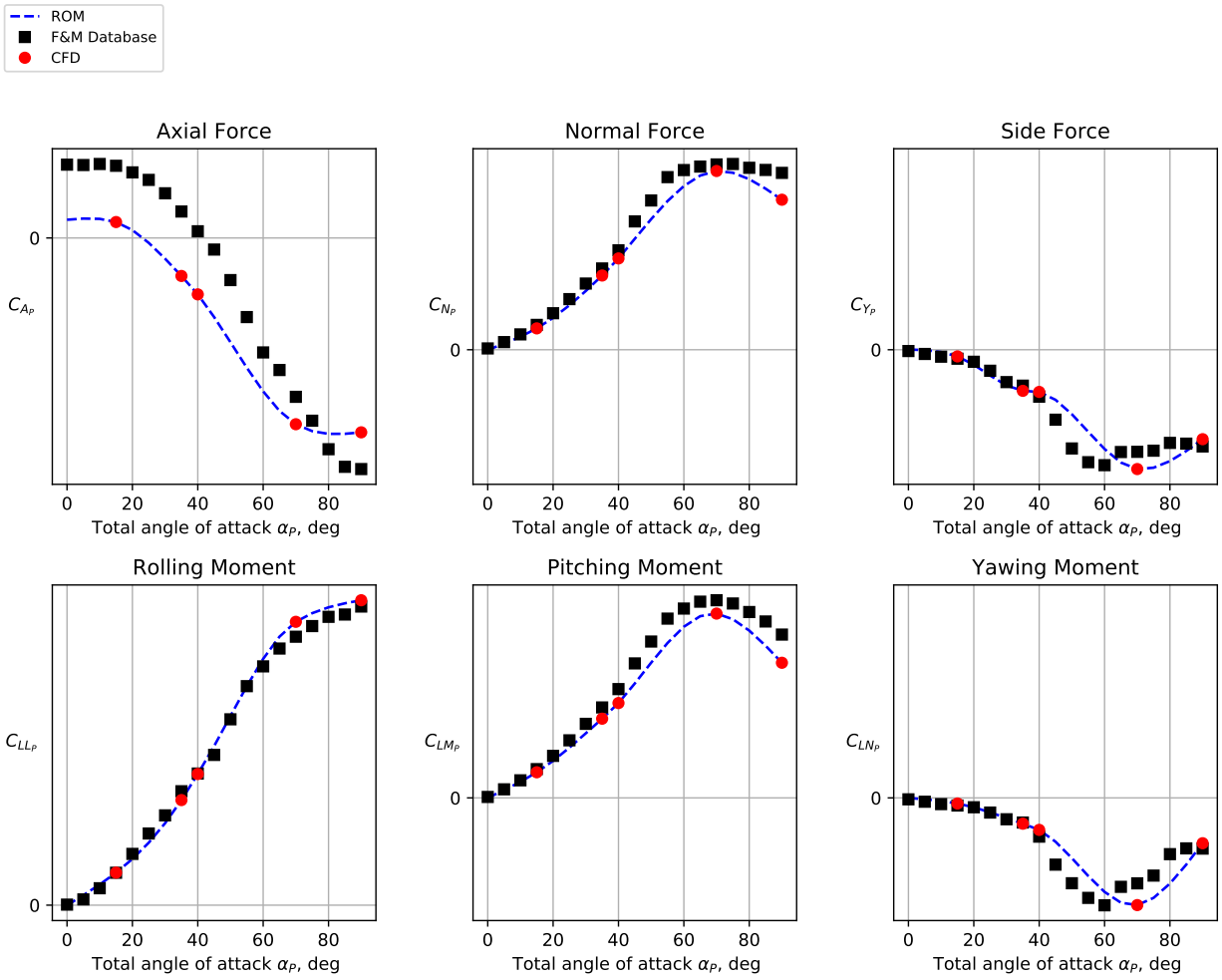

Fig. 12 Comparison of wind tunnel force and moment coefficients versus angle of attack at ϕ_P = 120° for the Block 1B cargo vehicle.

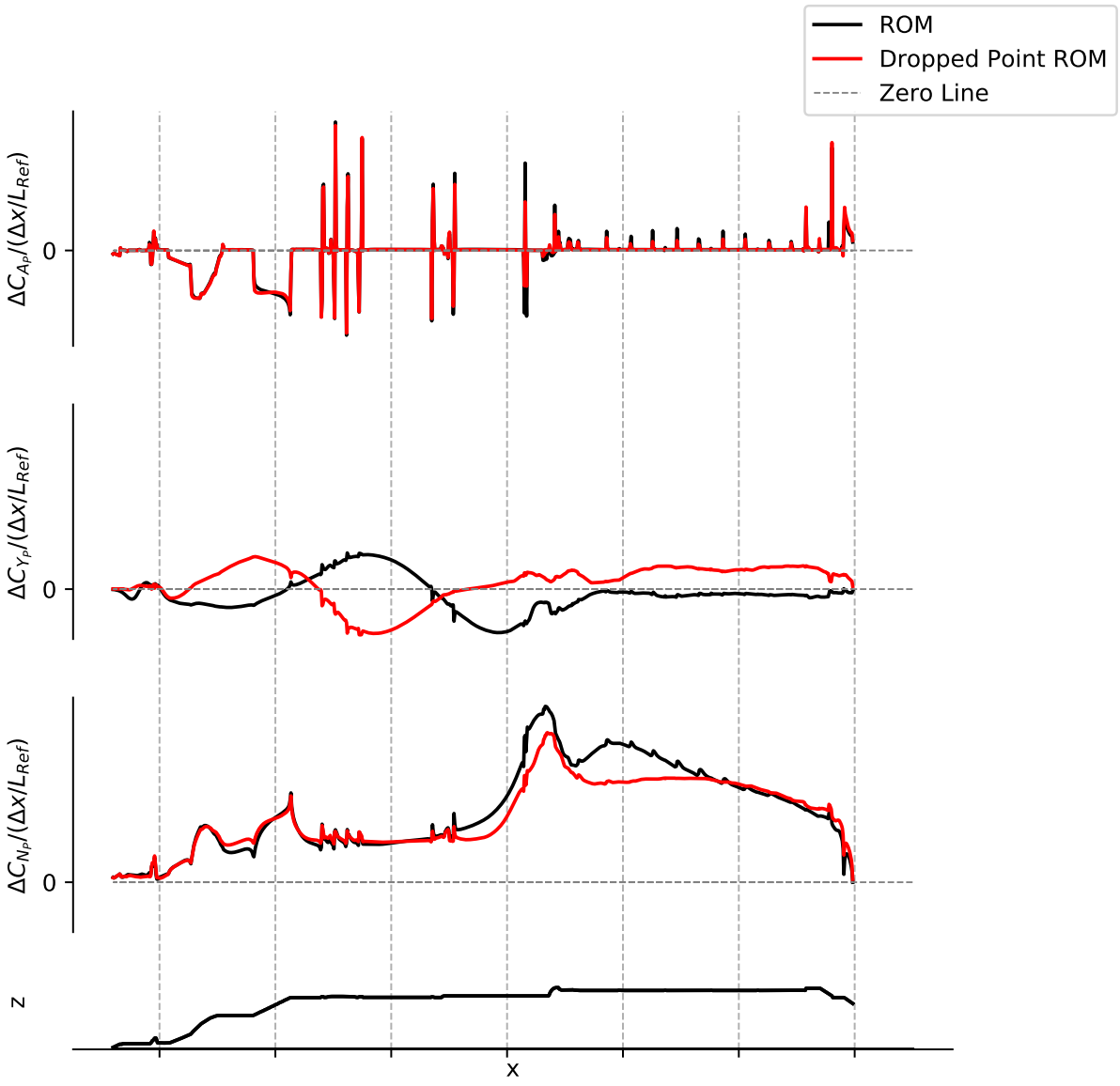

Fig. 13 LOO ROM lineloads for the core of the Block 1B crew configuration at $\alpha_P = 50°$, $\phi_P = 0°$.

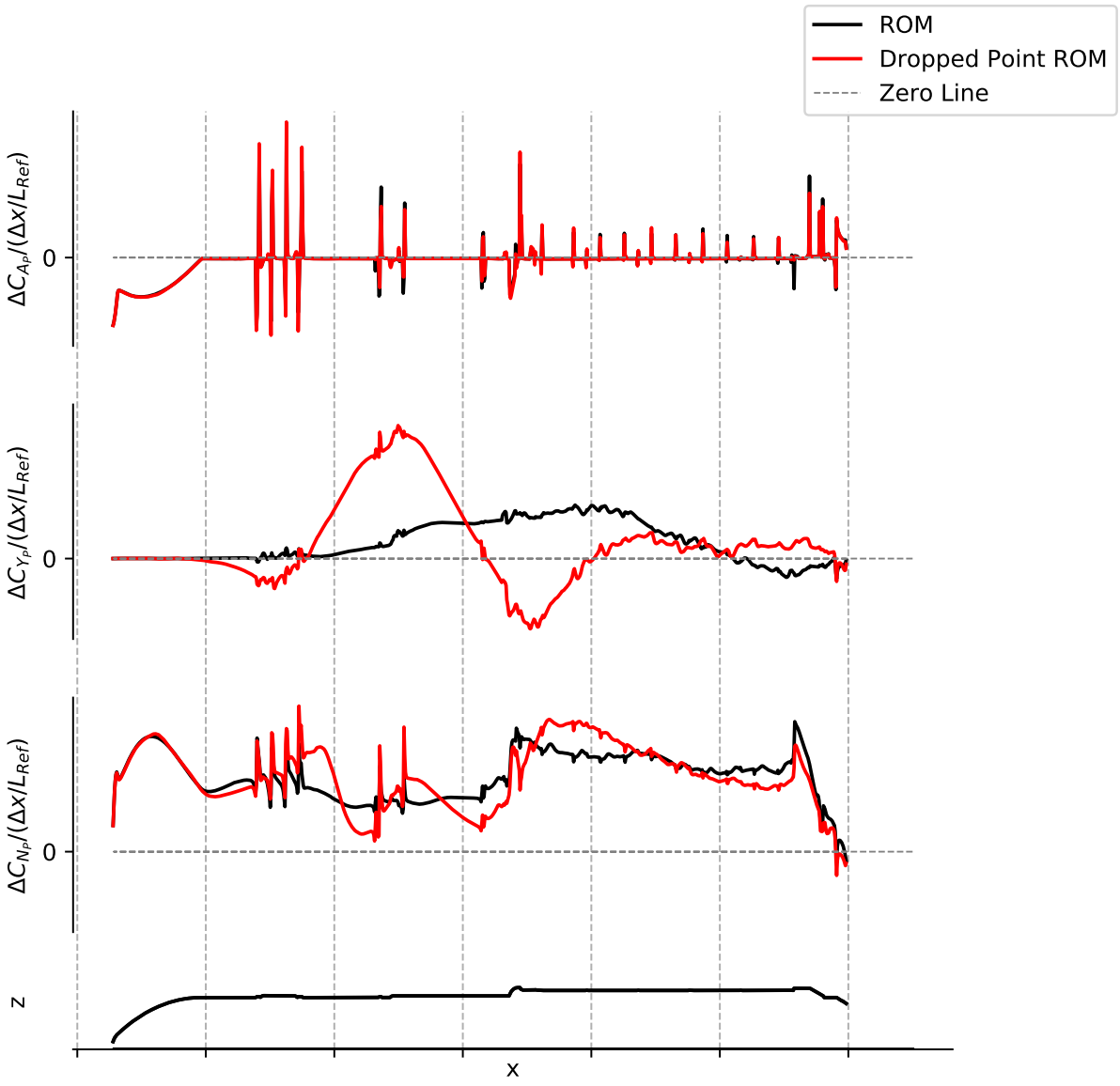

Fig. 14 LOO ROM lineloads for the core of the Block 1B cargo configuration at $\alpha_P = 45°$, $\phi_P = 270°$.

IV. Data Fusion

The data fusion method developed here takes the model as described in section III.A and finds a new set of data-fused ROM coefficients (called DFROM coefficients after adjustment) that forces the generated surfaces to integrate to desired forces and moments. As stated previously, while CFD is fairly trusted, it historically proves unreliable for flows with massive separation such as this problem and as such the wind-tunnel-derived force and moment database is considered higher fidelity than the CFD data. This inadequacy of CFD is displayed in the previous section particularly Fig. 11 where the CFD and as a result the ROM had difficulties in matching the integrated forces and moments seen in the wind tunnel. The goal is to develop a method to modify the ROM such that the integrated forces and moments match the values from the wind-tunnel-derived force and moment database without significant changes to the ROM lineloads.

A. Data Fusion Development

Since there are many coefficients that can be changed and only a handful of constraints, methods for constrained optimization were explored with the method of Lagrange multipliers being selected due to its simplicity.

The straight forward part of setting up the constrained optimization problem is determining the constraints. Since each component is analyzed separately, the superscript denoting component, k, will be dropped in this section. For force (or moment) j, the constraint is defined as:

$$\sum_{i=1}^{npc}\sum_{l=1}^{nvar} \hat{a}_i^l \Delta c_{i,j}^l - C_{F_j} = 0 \tag{5}$$

where $\hat{a}_i^l$ are the new DFROM coefficients of the i^{th} PC related to variable l and $\Delta c_{i,j}^l$ are the integrated j^{th} force (or moment) values of the i^{th} PC related to variable l. The higher fidelity force or moment data are represented by C_{F_j}, which are the j^{th} force (or moment) values from the database. This ensures that the new coefficients of the DFROM return surfaces and lineloads that integrate to force and moment database values. Because of the difference in asymmetric vortex behavior between the Block 1B cargo and crew configurations, the forces and moments used for constraints varied slightly. For the Block 1B crew configuration, all force and moment constraints were used. For the Block 1B cargo configuration, side force and yawing moment were not constrained for the core vehicle but all six were used for the SRBs. For the Block 1B cargo configuration, only the normal force and pitching moment were constrained for the core vehicle but all six were used for the SRBs. This does not substantially change the methodology but does show the flexibility and ease of adding or removing constraints.

After determining the constraints, a cost function was defined to complete the optimization. Three characteristics were decided on as important for a cost function. First, since the ROM produces physically plausible results, it is undesirable to stray far from the initial ROM coefficients. Large changes in the coefficients represent large changes to the output lineloads; which while not as accurate as desired, are the best spatially distributed data available. Second, a cost function that is easy to use with the method of Lagrange multipliers and to differentiate with respect to the DFROM coefficients is desired. Third, since the PCs contain differing amounts of variance in the system, a PC weighting term was introduced.

Given the above characteristics, the cost function developed for this work was:

$$f_{cost} = \sum_{i=1}^{npc}\sum_{l=1}^{nvar} w_i^l (a_i^l - \hat{a}_i^l)^2 \tag{6}$$

where w_i^l is a weighting term that allows for different PCs to be adjusted based on their relevance. Several options were explored for the weighting term before settling on using the corresponding eigenvalues from the PCA. This favored small changes to the PCs that correspond to large amounts of variance in the space, while allowing large changes in the PCs that contribute small amounts of variance to the space. This weighting proved most reliable in maintaining the overall shape of the lineloads without additional complexities.

Once the constraints and cost function are in place, the constrained optimization problem can be solved. As mentioned earlier, the method of Lagrange multipliers is used. To give a brief overview, the constraints are multiplied by new variables, λ_j, which are called the Lagrange multipliers and then added to the cost function to create the Lagrange function.

$$L = \sum_{j=1}^{ncon} \lambda_j \left[\sum_{i=1}^{npc}\sum_{l=1}^{nvar} \hat{a}_i^l \Delta c_{i,j}^l - C_{F_j} \right] - f_{cost} \tag{7}$$

The solutions to the problem are then found to be at the stationary points of this new equation. The stationary points are defined as the points where all the partial derivatives of a given function are zero, so the next step is to calculate all the partial derivatives and set them to zero.

The partial derivative with respect to the Lagrange multipliers, which represents the constraints has the form:

$$\frac{\partial L}{\partial \lambda_j} = \lambda_j \sum_{i=1}^{npc} \sum_{l=1}^{nvar} \hat{a}_i^l \Delta c_{i,j}^l - C_{F_j} \tag{8}$$

while the partial derivates with respect to the DFROM coefficients have the form:

$$\frac{\partial L}{\partial \hat{a}_i^l} = 2 * w_i^l (a_i^l - \hat{a}_i^l) + \sum_{j=1}^{ncon} \lambda_j \Delta c_{i,j}^l. \tag{9}$$

Because of the choice in cost function, the DFROM coefficients can be solved relatively easily. After setting the above equations to zero, a system of linear equations is formed with the unknowns being the Lagrange multipliers, λ, and the DFROM coefficients $\hat{a}$.

Once the new DFROM coefficients are determined, the model in equation 4 is used the same way as the original ROM but with the new DFROM coefficients. With this new adjustment, the surfaces generated by the new model will integrate to match the more trusted source of wind-tunnel data.

B. Results

Since the DFROM works by adjusting the ROM coefficients, it is important to see the changes that they undergo. A side by side comparison of the ROM and DFROM coefficients for the first pressure coefficient of the Block 1B cargo vehicle can be seen in Fig. 15. The left most graph is the original ROM coefficient as seen before and the center is the new DFROM coefficient. These plots use the same contour scale. The third plot (on the right) is the the percent change of the two ROMs (i.e., the DFROM coefficient minus the ROM coefficient normalized by the ROM coefficient). Because the weighting term used in the adjustment is equivalent to the eigenvalue associated with the first PC, it is expected that this variable changes the least, which is confirmed in these plots. In the more extreme case, the coefficients associated with the friction components change a significant amount due to their much lower eigenvalues. This is presented in Fig. 16, which plots the coefficient values for the first PC associated with the Z direction of friction across the domain for the Block 1B cargo vehicle. While some of the friction coefficient values have changed significantly more than initially expected, they prevent large changes in the pressure, which has a larger effect on final lineloads and one of the goals is to minimize the change in the overall shape of the lineload between the ROM and DFROM. Consequently, the increase in viscous forces has been deemed an acceptable side effect.

As a quick check to confirm that the DFROM coefficients are creating surfaces with the desired values, the forces and moments can be plotted against the wind tunnel as done previously. The forces and moments can be seen in Fig. 17 and Fig. 18, which shows the same conditions as were shown in the ROM section. Again while the rolling moment coefficient plot in Fig. 17 looks extreme, these values are relatively close to zero. The normal and pitching moment for the DFROM now match with the wind-tunnel-derived data for both configurations. Since the other four coefficients are allowed to drift for the Block 1B cargo configuration, they have slight changes, but overall they keep their values close to the ROM prediction as seen in Fig. 18

To show how the adjustment changes the surface prediction, two sets of three figures are used to show the ROM, DFROM and the difference between the two for a single condition. For the first set, an example from the Block 1B cargo vehicle at $\alpha_P = 75°$ and $\phi_P = 270°$ are shown. The first figure, Fig. 19, depicts the pressure distribution output by the ROM at α_P of 75° and a ϕ_P of 210°. The second figure, Fig. 20 is the equivalent DFROM surface, with the pressure delta (DFROM minus ROM) in Fig. 21. There is a slight decrease in pressure on the upper surface and a slight increase on the lower surface of the core, which may not look significant, but can significantly change the lineloads. On the SRBs, a much larger change can be seen near each nose, which is not unexpected because this is a region where the CFD has trouble. The effect of the slight change in surface pressure along the core can be analyzed in lineload form presented in Fig. 22. Here the ROM lineloads are in black, while the DFROM lineloads are in blue. The major difference is in the forebody, which points to significant underprediction in pitching moment as well as normal force in the ROM that is now corrected. This holds true to the general trend of the ROM underpredicting these two coefficients. The adjustments made have a slight effect on the side force sectional loads, which is expected from the constraints implemented for this vehicle.

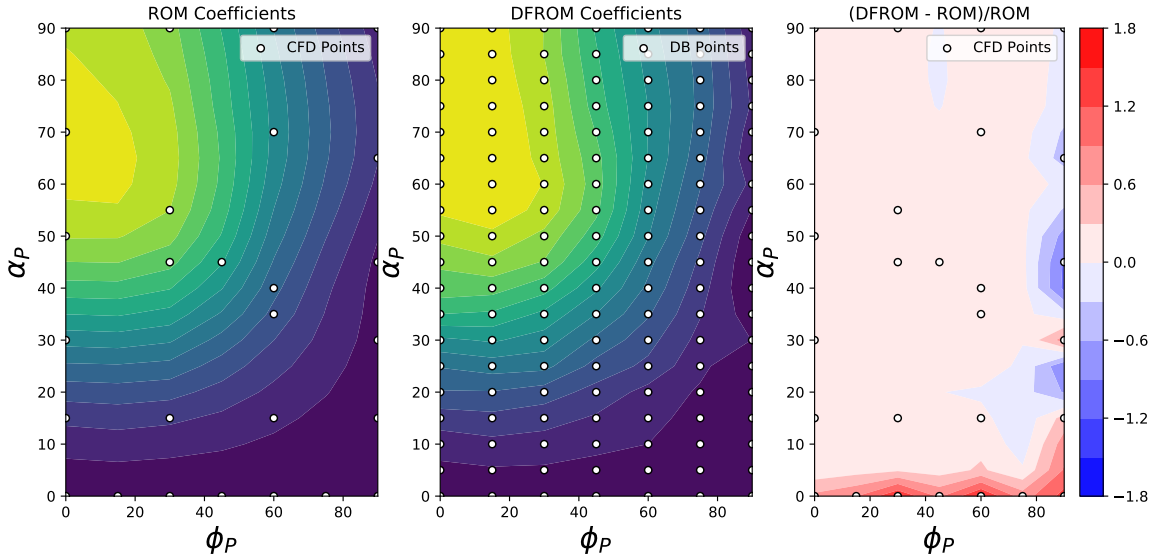

Fig. 15 Comparison of ROM and DFROM coefficients for first PC related to pressure for the core of the Block 1B crew vehicle.

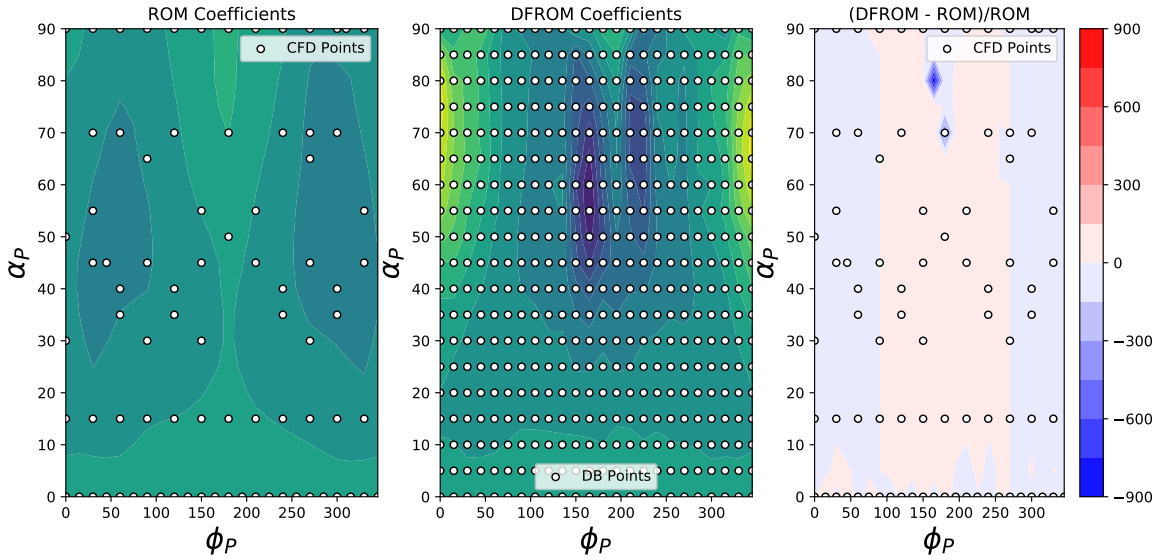

Fig. 16 Comparison of ROM and DFROM coefficients for first PC related to friction in the Z direction for the core of the Block 1B cargo vehicle.

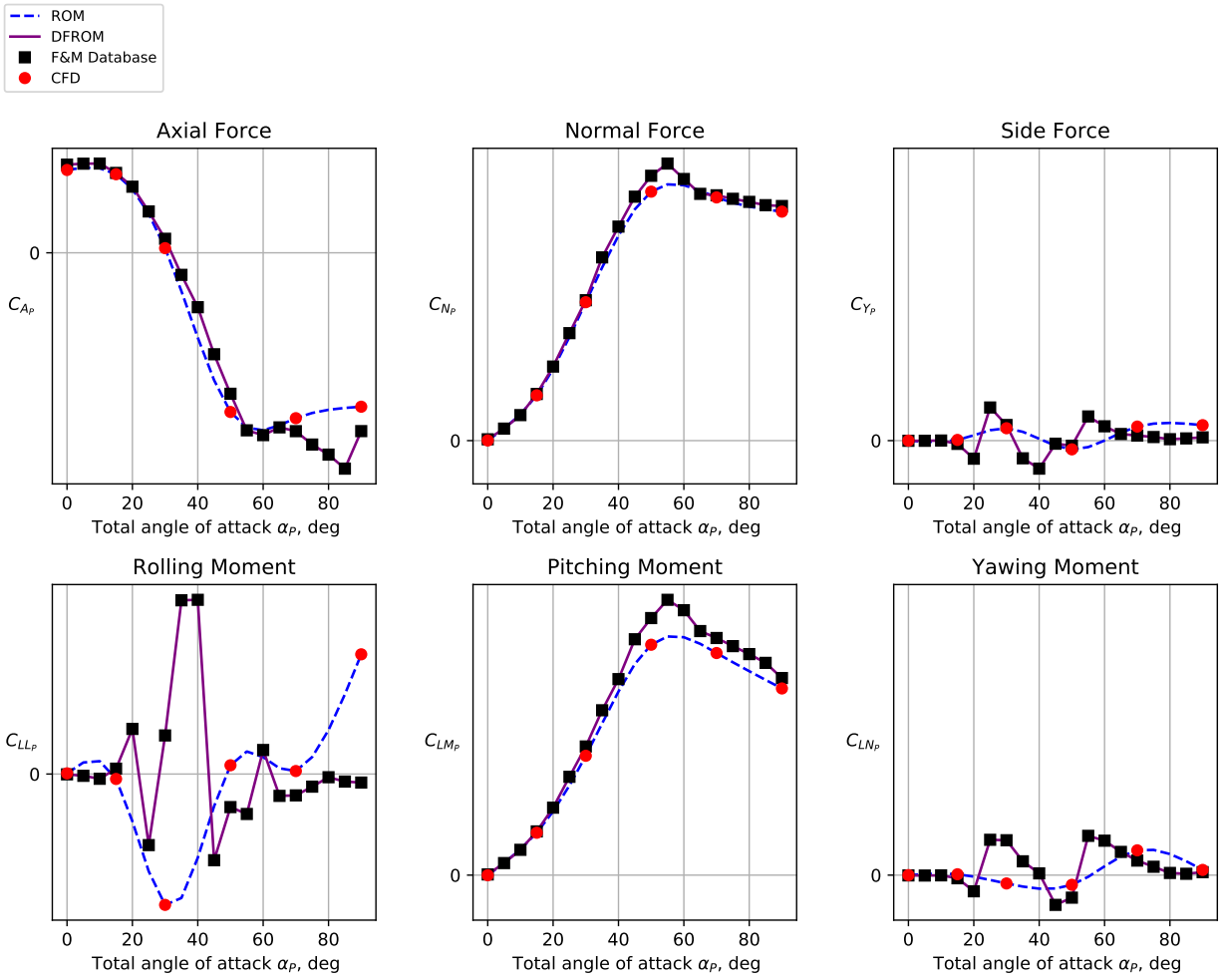

Fig. 17 Comparison of ROM force and moments to DFROM versus angle of attack at $\phi_P = 0°$ for the Block 1B crew vehicle.

The second set shows a more extreme change, which can be somewhat contributed to the asymmetric vortices, but not all of it. The next three figures show the Block 1B crew configuration at $\alpha_P = 40°$ and $\phi_P = 60°$. As before, the first figure, Fig. 23, shows the output of the ROM. Nothing sticks out here even when comparing to Fig. 24, which shows the DFROM results. However, the difference shown in Fig. 25 reveals significant areas of the pressure have been changed in order to meet the constraints. The good news is that when looking at the lineload level, Fig. 26, the adjustments are not that significant. Most of the adjustments on the core reflect a change in the side force. Here the ROM calculated a vortex on one side while the database shows a side force in the other direction. As the ROM and DFROM do not have a way to compensate for nonlinear effects, it creates these types of corrections. This type of correction exemplifies the strength of the DFROM adjustment method selected by demonstrating how even sign changes do not disrupt the basic structure of the lineload.

To show that the DFROM improves the predictive capability and robustness of the ROM, the LOO analysis was repeated. The same points as before were examined. The new dropped point DFROM was compared to the DFROM at the CFD condition that was dropped to examine its sensitivity to missing information. The first, Fig. 27, is the Block 1B crew vehicle at $\alpha_P = 50°$, $\phi_P = 0°$. The DFROM is the blue line and the dropped point DFROM is the red. The most significant change compared to the previous LOO analysis occurs at the aft end. Previously, there was a significant difference in the lineloads near the aft end particularly in sectional side force, which showed up as an offset. The sectional normal force is also more robust with a much smaller difference between the two DFROMs.

The second point, Fig. 28, is the Block 1B cargo vehicle at $\alpha_P = 45°$, $\phi_P = 270°$. This looks almost identical to

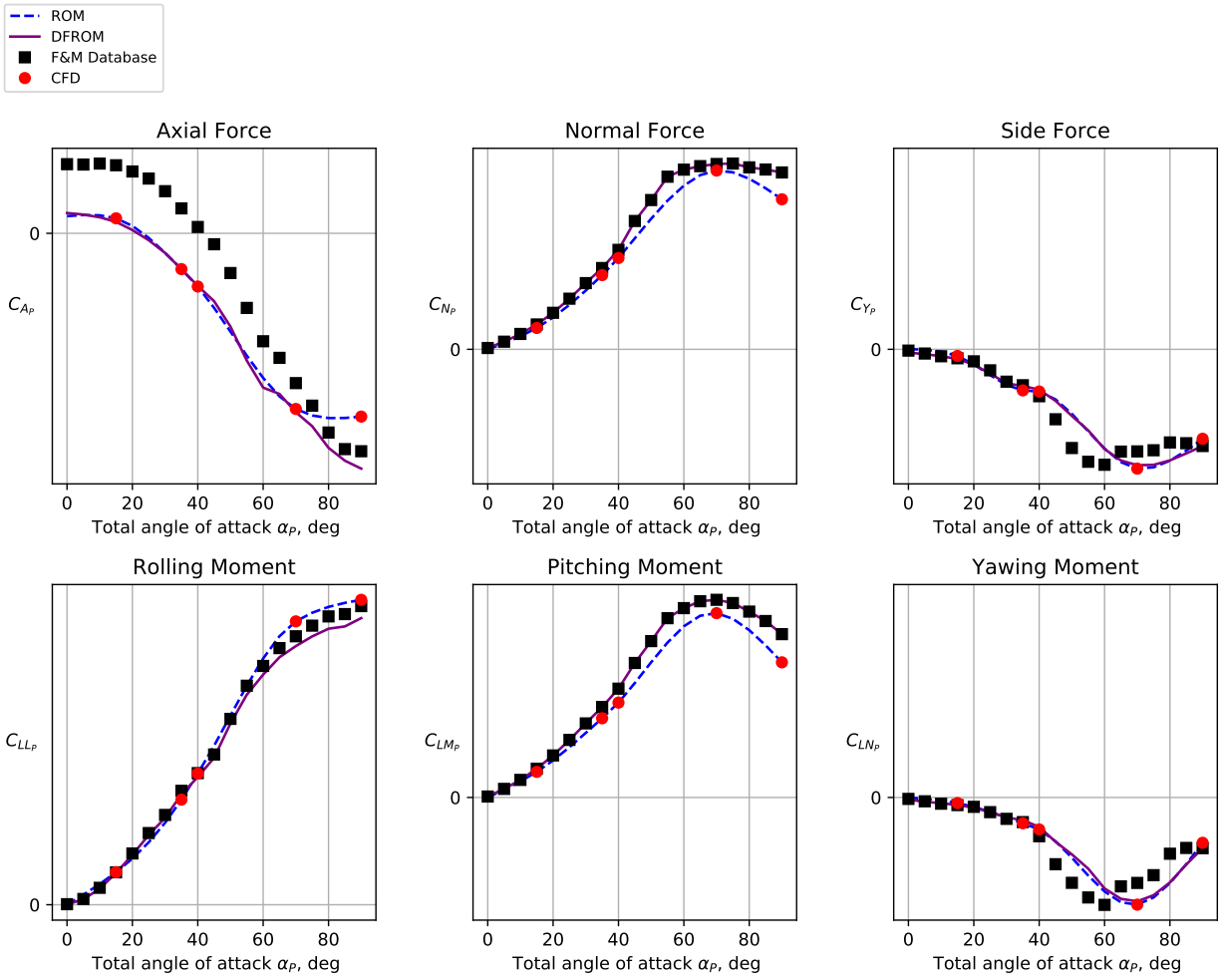

Fig. 18 Comparison of ROM force and moments to DFROM versus angle of attack at $\phi_P = 120°$ for the Block 1B cargo vehicle.

the LOO analysis done on the ROM. The differences are subtle but there is some movement in the lineloads near the aft end. This case points out one of the weaknesses in the adjustment method and difficulty in adjusting lineloads in general, which is that there are an infinite number of lines that integrate to any desired value. As before, these two sets of lineloads integrate to similar forces, which further reenforces this point. While the DFROM has the ability to help fill in some of the holes in the initial dataset, it lacks the ability to fill in "potholes".

The DFROM provides lineload results that are similar in shape and characteristic to the initial ROM output; however, they now integrate to the desired values. The DFROM output surfaces have similar characteristics to the ROM surfaces, which means they have similarities to the original CFD data. These DFROM lineloads tend to be a bit more robust to missing data but still not able to function without those essential data.

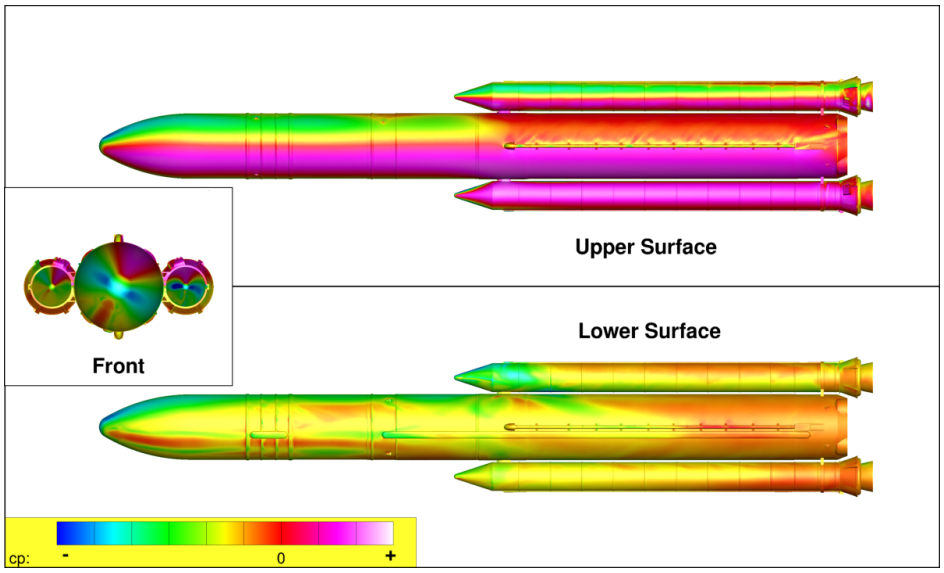

Fig. 19 ROM generated surface pressure distribution before adjustments for Block 1B cargo configuration at α_P = 75°, ϕ_P = 210°.

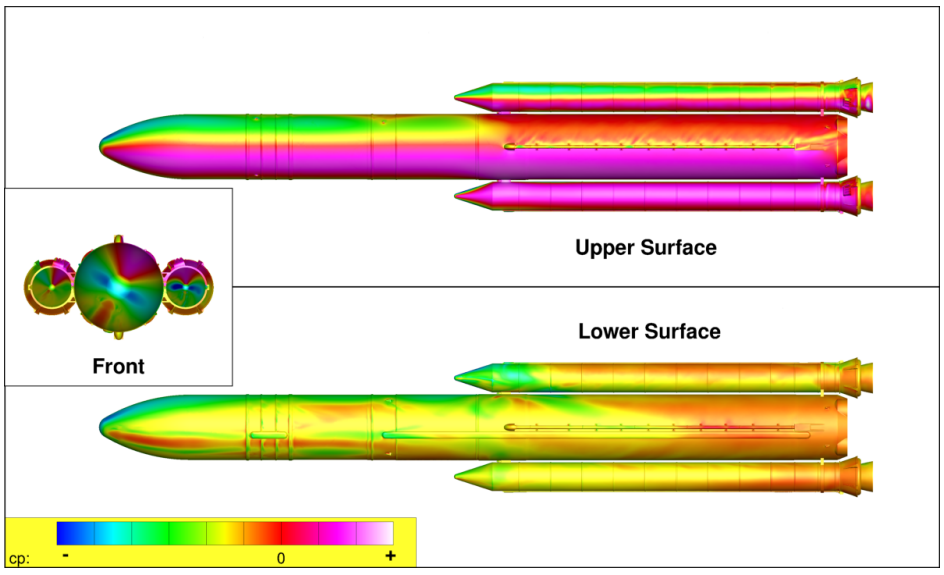

Fig. 20 DFROM generated surface pressure distribution after adjustments for Block 1B cargo configuration at α_P = 75°, ϕ_P = 210°.

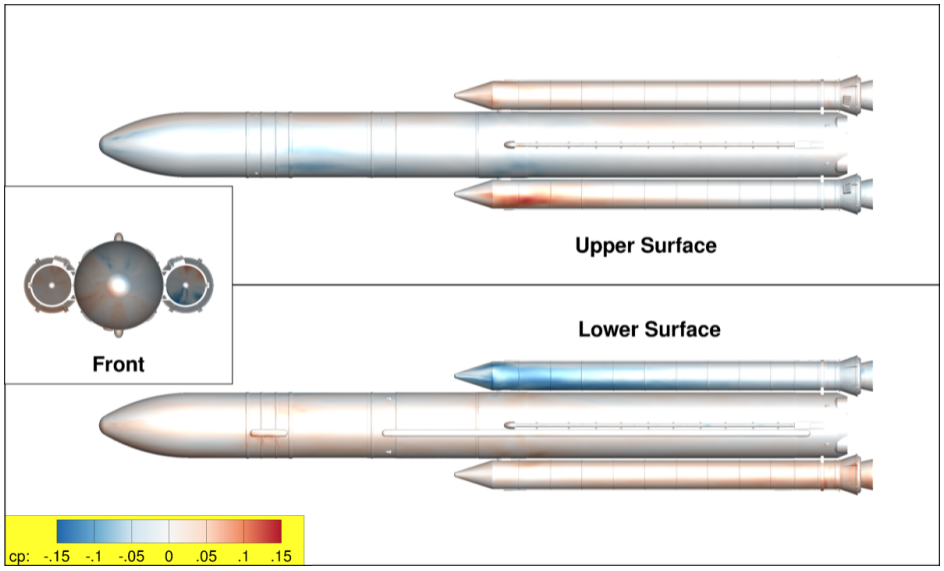

Fig. 21 Change in generated surface pressure distribution after adjustments for Block 1B cargo configuration at α_P = 75°, ϕ_P = 210°.

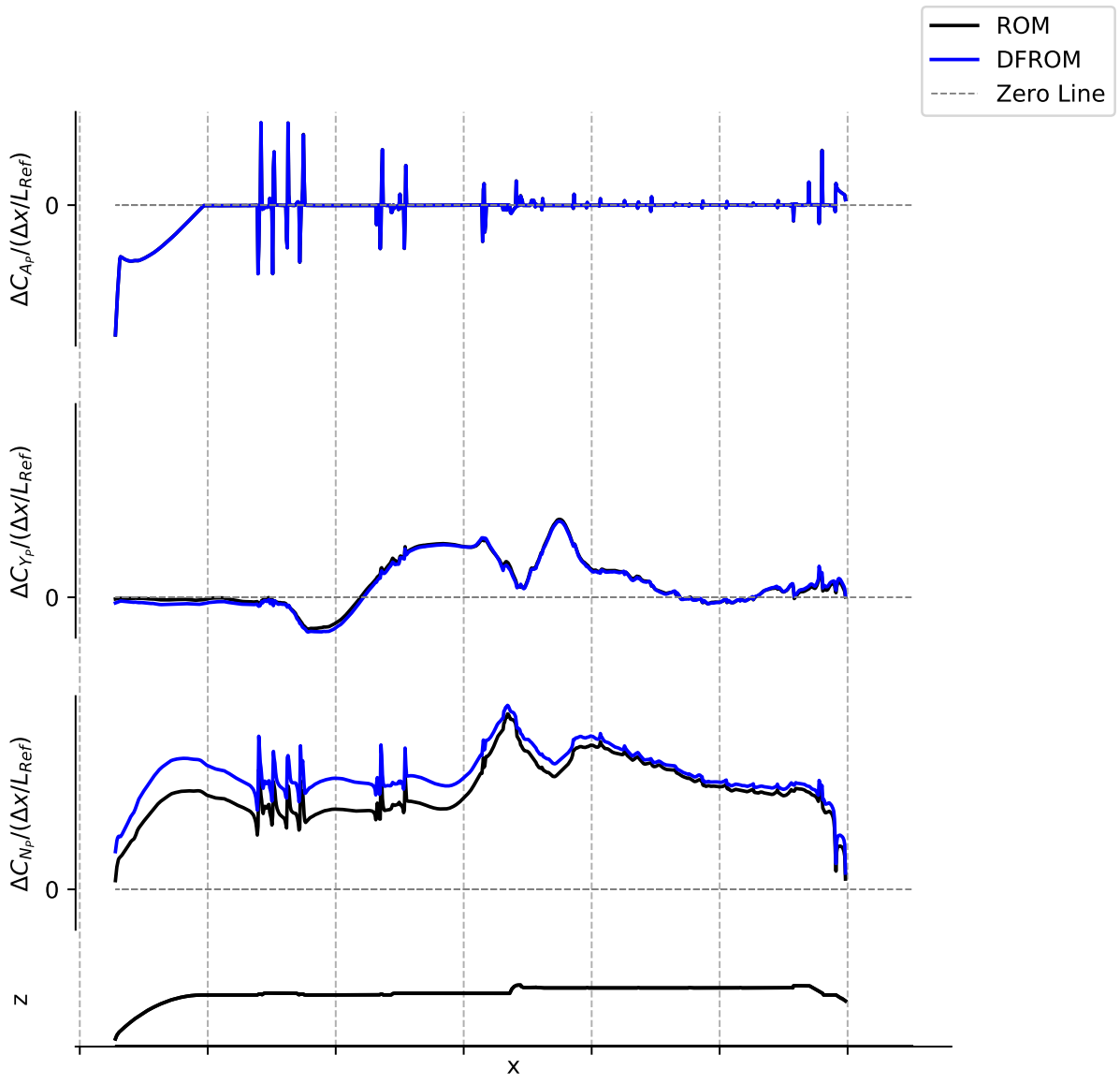

Fig. 22 Comparison between ROM and DFROM lineloads for the core of the Block 1B cargo configuration at α_P = 75°, ϕ_P = 210°.

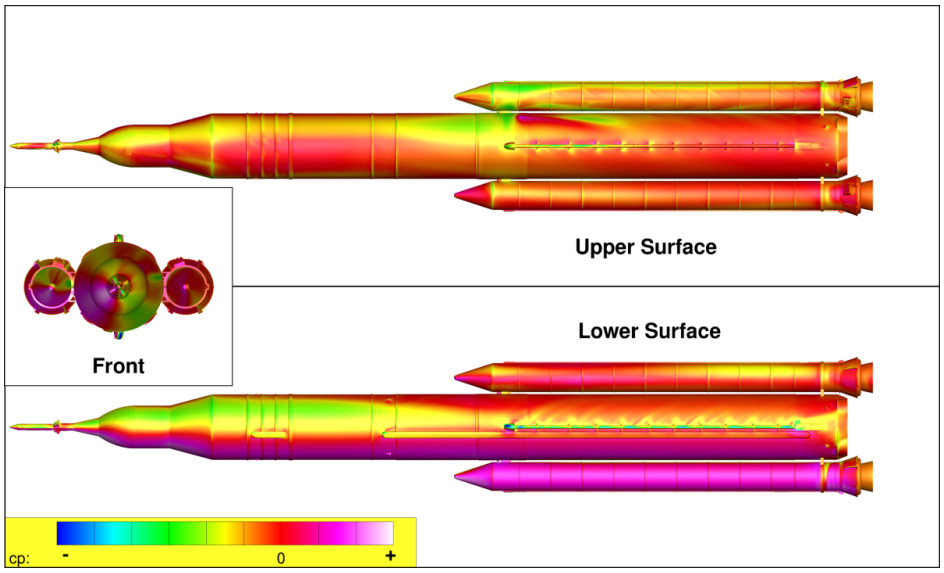

Fig. 23 ROM generated surface pressure distribution before adjustments for Block 1B crew configuration at $\alpha_P = 40°$, $\phi_P = 60°$.

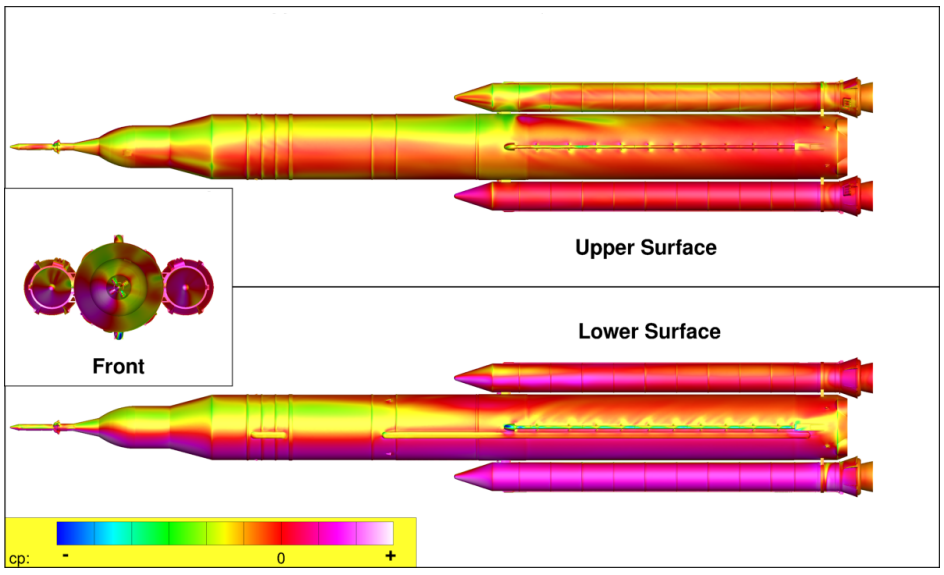

Fig. 24 DFROM generated surface pressure distribution after adjustments for Block 1B crew configuration at $\alpha_P = 40°$, $\phi_P = 60°$.

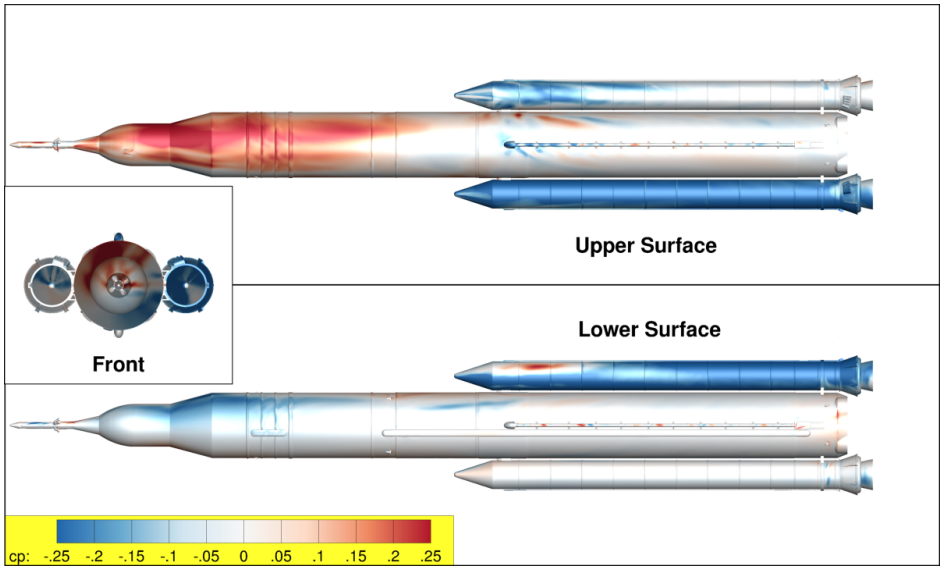

Fig. 25 Change in generated surface pressure distribution after adjustments for Block 1B crew configuration at α_P = 40°, ϕ_P = 60°.

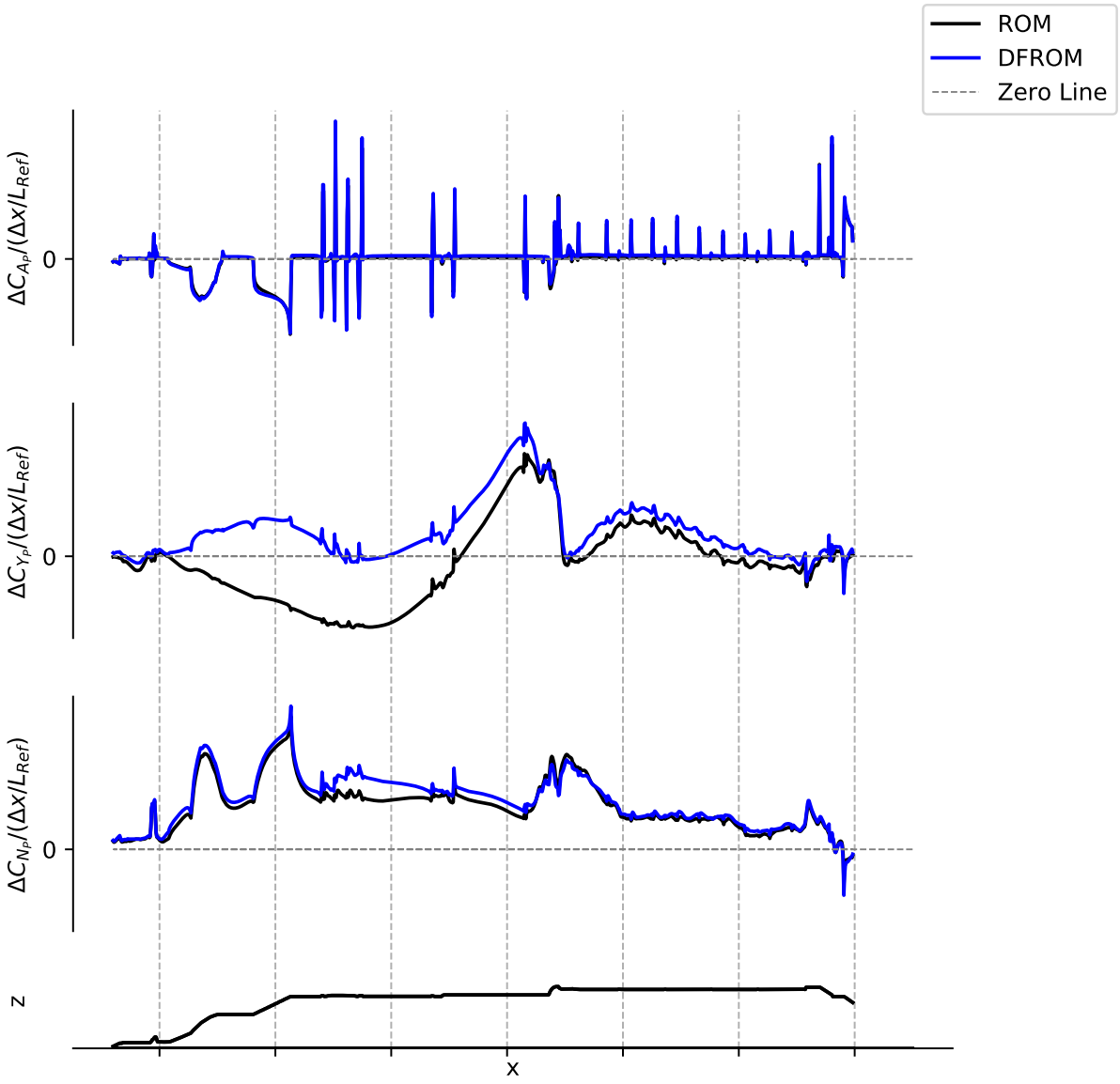

Fig. 26 Comparison between ROM and DFROM lineloads for the core of the Block 1B crew configuration at α_P = 40°, ϕ_P = 60°.

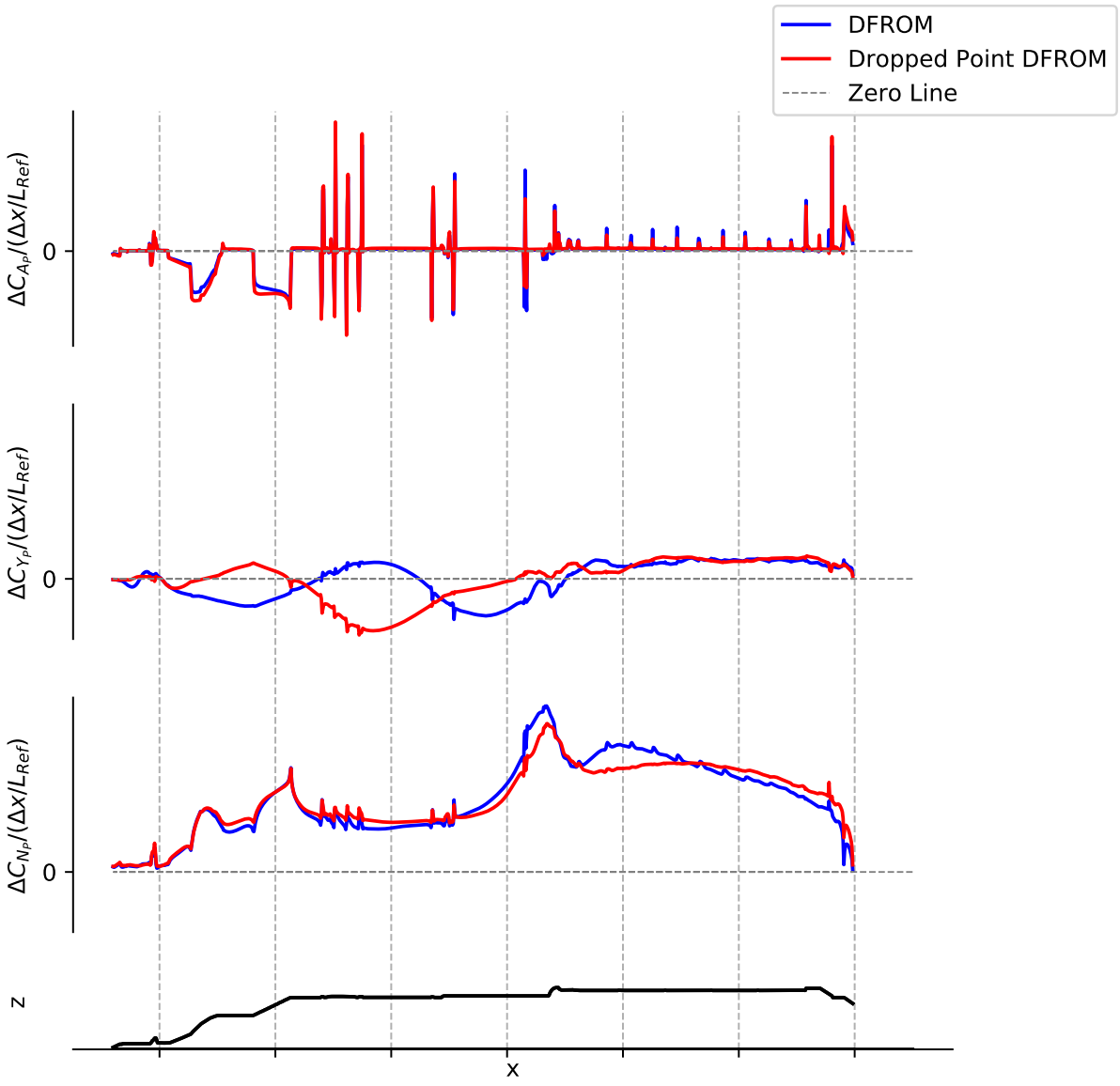

Fig. 27 LOO DFROM lineloads for the core of the Block 1B crew configuration at $\alpha_P = 50°$, $\phi_P = 0°$.

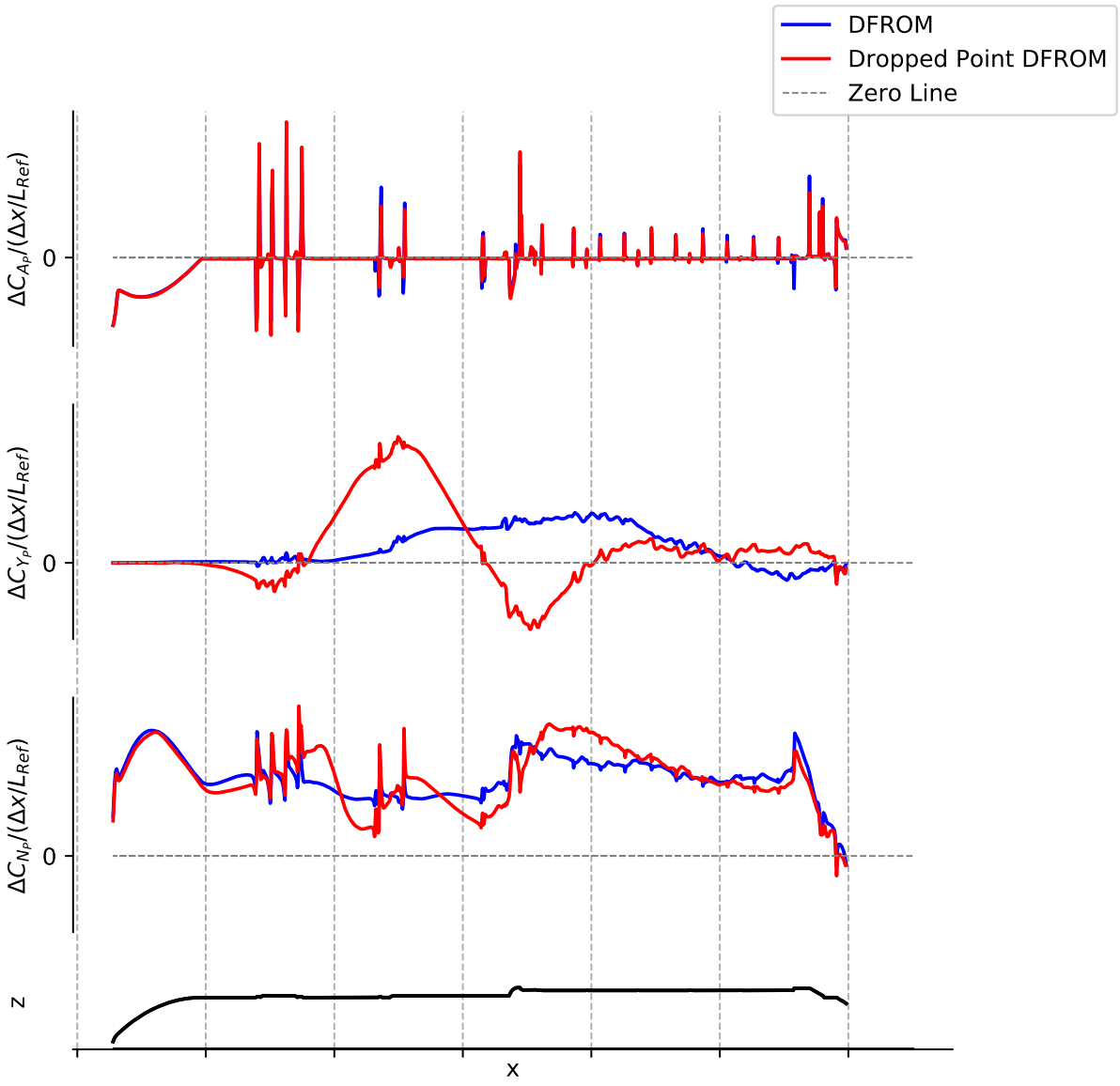

Fig. 28 LOO DFROM lineloads for the core of the Block 1B cargo configuration at α_P = 45°, ϕ_P = 270°.

V. Conclusion

The methods outlined above were used to develop and deliver a lineloads database for the SLS program to be used during the liftoff and transition regions of launch. A ROM was developed that significantly reduce the computational resources needed to calculate lineloads for the LOT domain. This ROM is able to output surfaces with comparable quality to CFD results, which means it inherits some of the limitations of CFD. These ROM techniques significantly speed up and reduce the cost of database development, but can also be used in exploratory design studies with the proper parameterization. By taking 21 points in one case and 60 points in another, the ROM generated values at 400+ database break points. After development of the ROM and satisfaction of its initial output, development shifted to data fusion techniques to overcome the shortcomings in the source data. The data fusion techniques allowed for a blending of the CFD-derived ROM with the more trusted force and moment data derived from wind tunnel testing. This ability allowed for distributed adjustments that solve some of the previous problems seen in lineload adjustments. Unlike the previous methods, this technique allows for adjustment of the whole surface, which couples changes in all forces and moments.

There are some limitations to the current technique though. The most significant is that PCA is a linear transformation and as such is not the best choice to capture effects that cannot be approximated linearly. Here, the biggest nonlinear effect that was encountered was the asymmetric vortices, although with enough data and some other mathematical manipulation, characterization is possible. In the end, these methods helped save millions of computation hours for the SLS program.

References

[1] Pinier, J. T., Herron, A. J., and Gomez, R. J., "Advances in the Characterization of NASA's Space Launch System Aerodynamic Environments," *57th AIAA Aerospace Sciences Meeting*, AIAA, 2019.

[2] Pandya, S., and Chan, W., *Computation of Sectional Loads from Surface Triangulation and Flow Data*, American Institute of Aeronautics and Astronautics, 2011. doi:doi:10.2514/6.2011-3680, URL `https://doi.org/10.2514/6.2011-3680`.

[3] Ratnayake, N. A., Krist, S. E., and Ghaffari, F., "Selection of Computational Fluid Dynamics Tools Used in Development of the Space Launch System Liftoff and Transition Lineloads Databases," *57th AIAA Aerospace Sciences Meeting*, AIAA, 2019.

[4] Carlson, H., Verberg, R., Pinier, J., and Krist, S. E., "Reduced-order Model for NASA Space Launch System Liftoff Aerodynamics," *AIAA 2015-0777*, 2015.

[5] Chan, D. T., and Paulson, J. W., "Aerodynamic Characterization and Improved Testing Methods for the Space Launch System Liftoff and Transition Environment," *57th AIAA Aerospace Sciences Meeting*, AIAA, 2019.

[6] Dalle, D. J., Rogers, S. E., Lee, H. C., and Meeroff, J., "Adjustments and Uncertainty Quantification for SLS Aerodynamic Sectional Loads," *2018 Applied Aerodynamics Conference*, American Institute of Aeronautics and Astronautics, 2018. doi:doi:10.2514/6.2018-3640, URL `https://doi.org/10.2514/6.2018-3640`.

[7] Fidler, J., and Bateman., M., "Asymmetric Vortex Effects on Missile Configurations," *Journal of Spacecraft and Rockets*, Vol. 12, No. 11, 1975, pp. 674–681.

[8] Hartwich, P., Hall, R., and Hemsch, M., "Navier-Stokes Computations of Vortex Asymmetries Controlled by Small Surface Imperfections," *AIAA 90-0395*, 1990.

[9] Morton, S. A., McDaniel, D. R., Sears, D. R., Tillman, B., and Tuckey, T. R., "Kestrel – A Fixed Wing Virtual Aircraft Product of the CREATE Program," *AIAA 2009-338*, 2009.

[10] Jolliffe, I., *Principal Component Analysis*, 2nd ed., Springer, 2002.